Charge-transfer-energy-dependent oxygen evolution reaction mechanisms for perovskite oxides

Wesley T. Hong[1], Kelsey A. Stoerzinger[1, §], Yueh-Lin Lee[2, #], Livia Giordano[2, 4], Alexis Grimaud[2, †, ◦], Alyssa M. Johnson[5], Jonathan Hwang[1], Ethan J. Crumlin[6], Wanli Yang[6], Yang Shao-Horn* [1, 2, 3]

[1] *Department of Materials Science and Engineering,*

[2] *The Research Laboratory of Electronics,*

[3] *Department of Mechanical Engineering, Massachusetts Institute of Technology, Cambridge, MA 02139, USA*

[4] *Dipartimento di Scienza dei Materiali, Università di Milano-Bicocca, Milano, Italy*

[5] *Department of Mechanical Engineering, University of St. Thomas, St. Paul, MN 55105, USA*

[6] *Advanced Light Source, Lawrence Berkeley National Laboratory, Berkeley, CA 94720, USA*

Current Address

[§] *Physical and Computational Sciences Directorate, Pacific Northwest National Laboratory, Richland, WA 99354, USA*
[†] *Chimie du Solide et de l'Energie, FRE 3677, Collège de France, 75231 Paris Cedex 05, France*
[◦] *Réseau sur le Stockage Electrochimique de l'Energie (RS2E), FR CNRS 3459, 80039 Amiens Cedex, France*
[#] *National Energy Technology Laboratory, Pittsburgh, PA 15236, USA*

Corresponding Author*

E-mail: shaohorn@mit.edu

Supplementary Methods

Soft X-ray spectroscopy analysis: Aligning XES, XAS, and XPS spectra and determining the experimental O 2p-band center

TM Lα and O Kα XES spectra were first aligned onto a common energy scale. The presence of hybridization features in the XES spectra imposes a physical constraint on the relative positions of the TM Lα and O Kα spectra. The feature positions were determined using spectral smoothing and differentiation. Minima in the second derivative were used to quantify the positions of features visible in the raw spectra, and the nearest local extrema in the first derivative were used to estimate the error in the feature position, requiring that a maximum be positive and minimum be negative; where this was not the case, the average error in feature position for a given spectrum was used.

Once aligned, the superposition of these spectra was aligned with XPS valence band measurements using the most prominent XPS valence band feature and the corresponding O K XES feature. Good agreement was found in the relative peak positions for the XPS and XES spectra, allowing for reliable deconvolution of the elemental parentage of valence band features and determination of band positions relative to the Fermi level. Note that due to ambiguity in the weighting of the XES spectra needed for the superposition, a 1:1 TM:O ratio was used, which will not reflect the absolute intensities of the XPS spectra. Applying an equivalent shift to the O K-edge XAS spectra as used in the XES spectra, this allows one to redefine the XAS and XES energy scales relative to the oxide Fermi level (as in **Fig. 2** and **Fig. 4**). Equivalently, this provides the energy of the Fermi level on the O K energy scale. The center of mass of the O Kα

XES spectra can then be calculated relative to the Fermi level to obtain an experimental measurement of the O 2*p*-band center.

More detailed discussion about the analysis is described elsewhere.[1]

Soft X-ray spectroscopy analysis: Determining the partial DOS relative to vacuum

The XES and XAS spectra for different oxide chemistries can be aligned onto a common, absolute energy scale by correcting the O K energy scale for the initial state differences in the O 1*s* core-hole energies (ΔV), which we estimated from the XPS O 1s binding energy shift (ΔE_B) after correcting for differences in relaxation effects (ΔR).[2, 3]

$$\Delta V = \Delta E_B + \Delta R \approx \Delta E_B + \frac{1}{2}\Delta\alpha$$

The Auger parameter, α, is defined as the sum of the O KL_2L_3 Auger electron kinetic energy and the O 1*s* XPS binding energy. When comparing the O K XES and XAS spectra of one oxide chemistry relative to another (the reference), a positive value of ΔV corresponds to a negative shift in the O K XES and XAS scale. After aligning the XES and XAS spectra of all oxides onto a common reference scale – in this case, $LaMnO_{3+\delta}$ – the energy scale was redefined relative to vacuum using experimental values of the work function; in this case, we took Φ = 4.5 eV for $LaMnO_{3+\delta}$.[4] More detailed discussion about the analysis is described elsewhere.[1]

Soft X-ray spectroscopy analysis: Extracting the charge-transfer energy

The distance between features in the XES and XAS spectra can be used to estimate the charge-transfer gap using the position of the O 2*p* nonbonding band and the lowest unoccupied energy state. From the XES and XAS spectra, peak B in the O Kα XES (**Fig. 2**) corresponds to the O 2*p* nonbonding band. The lowest unoccupied energy of the oxide is equivalent to its electron affinity. For conductive oxides, this is unambiguously the Fermi level and can be estimated by the combination of XPS and XES measurements.[1] For semiconducting oxides, the electron affinity can be extracted from the O K XAS pre-edge feature. We choose to use the pre-edge peak; this is necessarily larger than the true physical gap as it captures the difference in feature energies rather than band edges. Linear extrapolation or maxima in the second derivative were used previously to estimate the band edge from the pre-edge feature, but we caution that such analyses may convolute chemical trends of the ground state with excited state effects, which can include large variations if core-hole broadening varies substantially among the compounds studied. In our analysis, we treated $PrBaCo_2O_{5+\delta}$, $GdBaCo_2O_{5+\delta}$, $SmBaCo_2O_{5+\delta}$, $LaNiO_{3-\delta}$, and $La_{0.5}Sr_{0.5}CoO_{3-\delta}$ as conductors and the remainder as semiconductors based on previous studies of their transport properties.[5-7]

X-ray photoelectron spectroscopy: estimation of calibration errors

A set of C 1*s* and valence band measurements representative of the range of oxide chemistries studied here – $LaCoO_3$, $La_{0.8}Sr_{0.2}CoO_{3-\delta}$, $La_{0.5}Sr_{0.5}CoO_{3-\delta}$, and $PrBaCo_2O_{5+\delta}$ – were performed on Beamline 9.3.1 at the Advanced Light Source (Lawrence Berkeley National Laboratory). The measurements were performed at 4 keV incident photon energy to compare with lab-source XPS data (Al Kα, 1486 eV). Data from the two sets of measurements were both calibrated using the adventitious carbon peak of the C 1*s* spectra (E_B = 284.8 eV).[8] Information depths, taken as the distance necessary to collect 95% of the signal, were estimated using the inelastic-mean-free path (NIST Inelastic-Mean-Free Path Database, Gries G1 Equation).[9] This is approximately 8-9 nm for the Al Kα and 19-20 nm for the 4 keV measurements.

The valence band spectra are compared in **Fig. S3**. The spectra are fairly comparable with good agreement in the position of the high binding energy feature. The lower binding energy features are smeared when measured at 4 keV, indicating they may either be less sensitive to higher energy excitation (i.e. lower cross-section) and/or more localized at the surface. The primary difference is this smearing effect observed near the Fermi level; however, this is similar across the materials measured and indicates that errors are systematic across all materials. This gives us good confidence that the use of lab-source XPS data is reliable for capturing the Fermi level.

In addition, fitting the valence band edge using a complementary error function (a convolution of Heaviside step and Gaussian functions) with a constrained full-width-half-maximum (0.5 eV for the Al Kα and 2.3 eV for the 4 keV) can be used to estimate the position of the valence band edge. This yields a mean absolute error of 0.5 eV, which is comparable to calibration errors reported previously.[10] We take this 0.5 eV as the standard error of the experimental O 2*p*-band center, which is predominantly affected by the calibration error of the Fermi level.

Relationship between the charge-transfer energy and hybridization

The charge-transfer energy also controls the metal-oxygen hybridization of an oxide, which we probed using the pre-edge peak in the O K XAS data.[11] The metal-oxygen hybridizations of the oxides examined were found to scale inversely proportional to the charge-transfer energies (**Fig. S10**). Because the hybridization is determined by the ratio of the transfer integral (T_{pd}, related to the TM 3*d* – O 2*p* orbital overlap) to the charge-transfer energy of the metal-oxygen bond ($\beta \sim T_{pd}/\Delta$),[11, 12] the near-linear relationship indicates that the transfer integral remains largely unchanged across these oxides, and that the metal-oxygen hybridization is controlled primarily by the charge-transfer energy. The weak influence of the transfer integral on the metal-oxygen hybridization is also evident from the minor changes in hybridization among the rare-earth nickelates, RNiO$_3$ (R = La, Pr, Nd, Nd$_{0.5}$Sm$_{0.5}$, Sm, Eu, Gd),[11] for which the transfer integral varies but the charge-transfer energy remains similar.[13]

The Lankhorst model and its relationship with charge-transfer energy

The oxygen vacancy formation reaction is written in Kröger-Vink notation as:

$$2O_O^{\times} \rightarrow 2V_O^{q\cdot} + O_2 + 2qe' \qquad (1)$$

The term $O_O^{\times}$ refers to lattice oxygen sites, $V_O^{q\cdot}$ to oxygen vacancies with relative positive charge q relative to the filled state, and *e'* to the q electrons transferred in the anion oxidation reaction. The Lankhorst model for the oxygen vacancy formation energy (E_v) is correspondingly:

$$E_v = 2\varepsilon_{\{V_O^{q\cdot}\}} + 2q\varepsilon_{e'} \qquad (2)$$

where $\varepsilon_{\{V_O^{q\cdot}\}}$ is the energy of randomly distributed and noninteracting oxygen vacancy building units ($\{V_O^{q\cdot}\} = V_O^{q\cdot} - O_O^{\times}$),[14, 15] q is the effective ionic charge of the oxygen atoms in the oxide, and $\varepsilon_{e'}$ is the energy of the transferred electron. The first term is governed by the oxygen-site Madelung potential. Therefore, a good approximation for Eq. 1 is:

$$E_v \approx 2\big(-qeV_M(0)\big) + 2q\varepsilon_{e'} \quad (3)$$

where e is the elementary charge and V_M (O) is the oxygen-site Madelung potential. The O 2*p* non-bonding band position directly scales with the O 1*s* core level (the nearly constant O *Kα* emission energy of the band indicates that the O 2*p* → O 1*s* transition does not change, **Fig. S1**), which is entirely governed by the site Madelung energy;[16] therefore, the position of the O 2*p* non-bonding band provides direct information on the relative oxygen Madelung energy of an oxide. The latter term is determined by the lowest energy unoccupied state, which may be localized or itinerant depending on the oxide chemistry.[14, 17] For itinerant systems, the lowest energy state is given by the Fermi level.[14] For localized systems, the lowest energy state is given by the oxide electron affinity, which can be approximated from the O *K* XAS band position. From this, Eq. 3 can be rewritten as:

$$E_v \sim 2q\big(-\varepsilon_{O2p,\mathrm{nb}} + \varepsilon_F\big) \text{ for metals} \quad (4a)$$

$$E_v \sim 2q\big(-\varepsilon_{O2p,\mathrm{nb}} + \varepsilon_{O\,K\,XAS}\big) \text{ for semiconductors} \quad (4b)$$

The terms within the parentheses of Eq. 4a and 4b is precisely the definition of the charge-transfer energy using the XAS and XES data.

The point of zero charge and its relation to hydroxide affinity

The point of zero charge (pzc) of an oxide is defined as follows in the absence of adsorption of ions other than H^+ and OH^-:[18]

$$\text{pzc} = \frac{pK_{a_1} + pK_{a_2}}{2} \tag{5}$$

where K_{a_1} and K_{a_2} are the equilibrium constants of the proton affinity reactions

$$H^+ + A^- \rightleftharpoons HA \tag{6a1}$$

$$H^+ + HA \rightleftharpoons H_2A^+ \tag{6a2}$$

or analogously the hydroxide affinity reactions

$$OH^- + AOH \rightleftharpoons AO^- + H_2O \tag{7a1}$$

$$OH^- + A^+ \rightleftharpoons AOH \tag{7a2}$$

Reaction a_1 is associated with proton transfer between the negatively charged and neutral oxide surface sites, while reaction a_2 is associated with proton transfer between the neutral and positively charged oxide surface sites. The pzc is the average of these two acid-base reactions for the ensemble of surface sites[19] and indicates the pH where these two reactions result in a charge-neutral surface. Because the pK_a of each site is proportional to ΔG of the respective reaction, the pzc is an average energy of the two protonation/hydroxylation reactions among all surface sites, providing a direct measure of average proton/hydroxide affinity of the ensemble.[19]

Marcus models of sequential and concerted proton-electron transfer

For an arbitrary elementary step in the OER, equations for the four potential energy surfaces from Marcus models of the states[20] are defined as:

(initial state) $$E_1(q_e, q_p) = \lambda_e {q_e}^2 + \lambda_p {q_p}^2 + 2\bar{\lambda} q_e q_p$$

(proton transfer) $$E_2(q_e, q_p) = \lambda_e {q_e}^2 + \lambda_p (q_p - 1)^2 + 2\bar{\lambda} q_e (q_p - 1) + E_2^0$$

$$E_2^0 = HA(\text{surface})$$

(electron transfer) $$E_3(q_e, q_p) = \lambda_e (q_e - 1)^2 + \lambda_p {q_p}^2 + 2\bar{\lambda}(q_e - 1) q_p + E_3^0 + \eta$$

$$E_3^0 = EA(\text{surface}) + \Delta G_{\text{solv}}(\text{OH}^\bullet)$$

(final state) $$E_4(q_e, q_p) = \lambda_e (q_e - 1)^2 + \lambda_p (q_p - 1)^2 + 2\bar{\lambda}(q_e - 1)(q_p - 1) + \Delta G + \eta$$

$$\eta = e_0 \left(\phi - \phi^{\text{eq}}_{\text{A,H}^+/\text{HA}}\right)$$

$$\Delta G = HA + EA$$

where $q_{e,p}$ are the number of electrons/protons transferred, $\lambda_{e,p}$ is the reorganization energy of electrons/protons, $\bar{\lambda}$ is the coupling energy for proton and electron transfers, *HA*(surface) is the hydroxide affinity of the active site, *EA*(surface) is the electron affinity of the active site, and $\Delta G_{\text{solv}}(\text{OH}^\bullet)$ is the solvation energy of OH radicals. The potential energy surface for the reaction is then given by the minimum of these four functions.

Values of the reorganization energies were estimated from solvent behavior work by Auer et al.[21]: λ_e = 1.5 eV, λ_p = 0.5 eV, and $\bar{\lambda}$ = –0.5 eV. We assume the reorganization energy is predominantly determined by the solvent. Although these values may vary, the differences among the contour plots for the different oxides do not qualitatively change. In our analysis,

we've estimated hydroxide and electron affinities using the absolute band positions as determined in **Fig. 4**. Though not specific to any active site or intermediate species, these values serve as single-point estimates for the ensemble behavior of the surface.[22] The solvation energy of OH radicals was taken to be –0.4 eV.[23]

Potential and pH-dependence of sequential proton-electron transfer

A microkinetic model is shown to demonstrate the pH and potential dependence of a sequential proton-electron transfer in both the proton-limiting and electron-limiting cases for the elementary reaction $AH + OH^- \rightarrow A + H_2O + e^-$

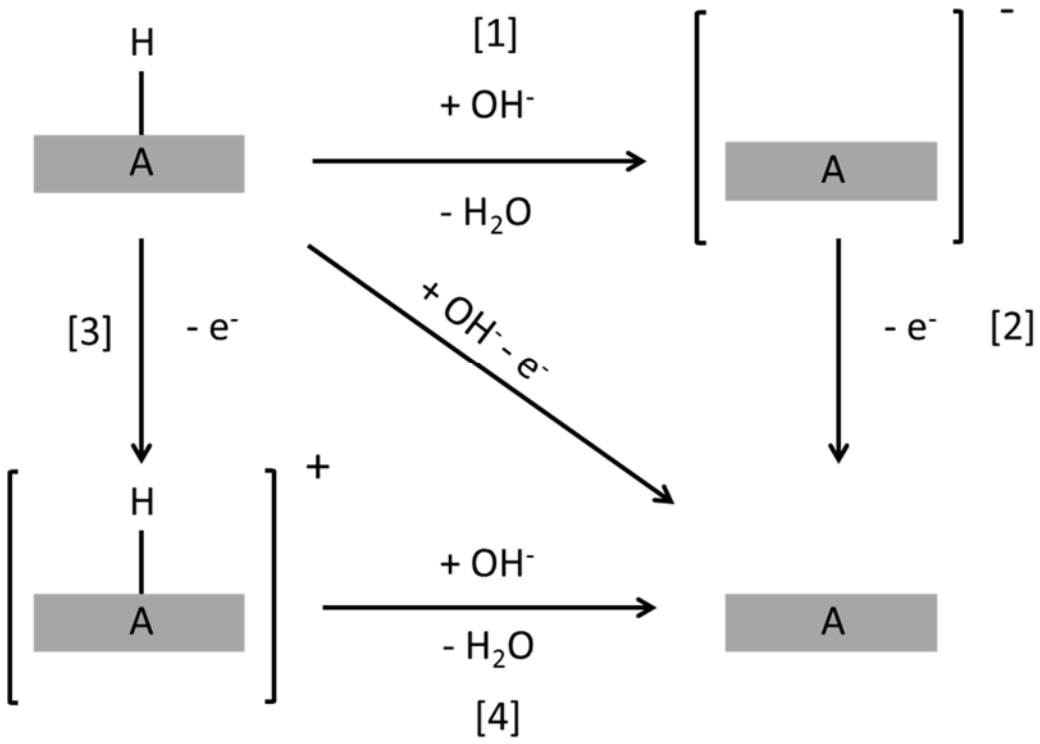

In the case that the proton and electron transfers are concerted (diagonal pathway), the rate is given as:

$$r = k^+[\mathrm{AH}][\mathrm{OH}^-]e^{\frac{(1-\alpha)F(E-E^0)}{RT}} - k^-[\mathrm{A}]e^{\frac{-\alpha F(E-E^0)}{RT}}$$

The presence of pH or potential dependence in the reaction rate when measured against the reversible hydrogen electrode is determined by the pH dependence of the pre-factors, k, and potential dependence of the exponential terms. The pH dependence explicit in the coefficients is

present when measuring kinetic current against the standard hydrogen electrode, but falls out when compared to the reversible hydrogen electrode. Therefore, in a concerted proton-electron transfer, there is only potential dependence in the reaction rate (red terms) when measuring on the reversible hydrogen electrode scale.

In contrast, both the electron-transfer limited path (steps 1 and 2, where 2 is the rate-limiting step) and proton-transfer limited path (steps 3 and 4, where 4 is the rate-limiting step) exhibit pH dependence (blue) and potential dependence (red):

$$r_{1,2} = k_2^+ k_1^+ / k_1^- [\mathrm{AH}][\mathrm{OH}^-] e^{\frac{(1-\alpha_2)F\left(E-{E_2}^0\right)}{RT}} - k_2^- [\mathrm{A}] e^{\frac{-\alpha_2 F(E-{E_2}^0)}{RT}}$$

$$r_{3,4} = k_4^+ k_3^+ / k_3^- [\mathrm{AH}][\mathrm{OH}^-] e^{\frac{F\left(E-{E_3}^0\right)}{RT}} - k_4^- [\mathrm{A}]$$

The consequence is that these reactions have a change in reaction rate as pH is changed and overpotential is fixed relative to the reversible hydrogen electrode, in addition to potential dependence (Tafel slope). The reaction orders on pH are illustrated in ESI **Fig. S22**.

Role of the charge-transfer energy in activating lattice-oxygen sites

We also expect that strong covalency will increase the redox activity of oxygen sites in addition to metal sites due to the large O 2*p* character of electronic states near the Fermi level (ESI **Fig. S20**) for the alkaline OER.[12] This redox activity of oxygen can facilitate the formation of peroxo- and/or superoxo-like species on the surface (i.e. $(O_2)^{n-}$ / O_2),[24] similar to oxygen evolution in a solid oxide electrolytic cell (e.g. O−M−O → □−M−OO + $2e^-$). This proposed oxygen participation is distinct from the involvement of active vacancy sites[25] or the oxygen intercalation reaction in oxygen-deficient oxides[26] (e.g. $ABO_{3-\delta} + 2\delta OH^- \rightarrow ABO_3 + \delta H_2O + 2\delta e^-$), which still involve redox of the cation and do not form O–O bonds using the lattice oxygen. Chemical trends in the thermodynamic barrier for peroxo-/superoxo- formation of different oxides can be measured by the enthalpy of the oxygen vacancy formation reaction ($2O_O^\times \rightarrow 2V_O^{\cdot\cdot} + O_2 + 2e'$, in Kröger-Vink notation), for which the formation of a peroxo-/superoxo- species from lattice oxygen is a necessary reaction step. The vacancy formation energetics are directly controlled by the charge-transfer energy because it defines the energy for metal-to-oxygen electron transfer[27, 28] (see ESI for detailed discussion). We find that decreasing the charge-transfer energy is associated with a reduction in the enthalpy of oxygen vacancy formation[29-33] (ESI **Fig. S11**), indicating that highly covalent oxides are more capable of forming peroxo-/superoxo- species. The origin of these different reaction mechanisms can be seen directly in the electronic structure, where LSCO50 and PBCO represent substantially lower charge-transfer energy (i.e. more covalent M−O bonds) that enable the oxygen atoms to serve as active sites. Increasing the Sr content is expected to further lower the charge-transfer energy, and $SrCoO_{3-\delta}$ was previously found to form peroxo-/superoxo- like species by directly evolving oxygen through the combination of neighboring oxygen atoms in the perovskite lattice.[34] This relationship between the activation of

lattice oxygen in the OER mechanism and charge-transfer energy is consistent with the role that higher covalency plays in stabilizing Group VI element dimerization, as studied extensively for forming $(X_2)^{2-}$ (X = S, Se, Te) in dichalcogenides.[35] Therefore, the redox activity of lattice oxygen is expected to contribute more significantly to the OER kinetics in oxides with low charge-transfer energies, such as oxides with Co^{4+} and Ni^{3+}.[34, 36]

Table S1 | Summary of lattice parameters from profile fitting (FullProf) of the oxides in this work. Oxide abbreviations: $La_{0.8}Sr_{0.2}CoO_{3-\delta}$ (LSCO20), $La_{0.5}Sr_{0.5}CoO_{3-\delta}$ (LSCO50), $GdBaCo_2O_{5+\delta}$ (GBCO), $SmBaCo_2O_{5+\delta}$ (SBCO), $PrBaCo_2O_{5+\delta}$ (PBCO), $Ba_{0.5}Sr_{0.5}Co_{0.8}Fe_{0.2}O_{3-\delta}$ (BSCF).

Oxide	**Symmetry**	***a* (Å)**	***b* (Å)**	***c* (Å)**	**A**	**β**	**γ**
$LaCrO_3$	$Pnma$	5.575	7.760	5.483	90°	90°	90°
$LaMnO_{3+\delta}$	$R\bar{3}c$	5.528	5.528	13.340	90°	90°	120°
$LaFeO_3$	$Pnma$	5.566	7.853	5.554	90°	90°	90°
$LaCoO_3$	$R\bar{3}c$	5.443	5.443	13.092	90°	90°	120°
$LaNiO_{3-\delta}$	$R\bar{3}c$	5.456	5.456	13.165	90°	90°	120°
LSCO20	$R\bar{3}c$	5.442	5.442	13.179	90°	90°	120°
LSCO50	$R\bar{3}c$	5.421	5.421	13.246	90°	90°	120°
GBCO	$Pmmm$	3.912	3.876	7.533	90°	90°	90°
SBCO	$Pmmm$	3.910	3.888	7.565	90°	90°	90°
PBCO	$P4/mmm$	3.906	3.906	7.632	90°	90°	90°
BSCF	$Pm\bar{3}m$	3.982	3.983	3.982	90°	90°	90°

Table S2 | Average specific surface areas as measured by up to three independent Brunauer-Emmet-Teller (BET) single-point analyses. Oxide abbreviations: $La_{0.8}Sr_{0.2}CoO_{3-\delta}$ (LSCO20), $La_{0.5}Sr_{0.5}CoO_{3-\delta}$ (LSCO50). First measurements were performed after 12 hours degassing at 150 °C. Subsequent measurements were performed after 3 hours degassing at 150 °C. Deviations were consistently observed to be less than 20%.

Oxide	**BET surface area (m^2/g)**
$LaCrO_3$	1.28
$LaMnO_{3+\delta}$	0.26
$LaFeO_3$	0.39
$LaCoO_3$	0.42
$LaNiO_{3-\delta}$	1.41
LSCO20	0.37
LSCO50	0.35

Table S3 | Summary of key soft X-ray spectroscopy parameters for the oxides in this work. Oxide abbreviations: $La_{0.8}Sr_{0.2}CoO_{3-\delta}$ (LSCO20), $La_{0.5}Sr_{0.5}CoO_{3-\delta}$ (LSCO50), $GdBaCo_2O_{5+\delta}$ (GBCO), $SmBaCo_2O_{5+\delta}$ (SBCO), $PrBaCo_2O_{5+\delta}$ (PBCO), $Ba_{0.5}Sr_{0.5}Co_{0.8}Fe_{0.2}O_{3-\delta}$ (BSCF). The charge-transfer energy, Δ, was computed from the difference in EA and NB in the case of semiconductors,[1] and E_F and NB in the case of conductors.

Oxide	**NB**	**IE**	**EA**	E_F	**O 1*s* XPS BE**	**O KLL KE**
$LaCrO_3$	7.0	5.1	−0.1	4.3	528.4	513.4
$LaMnO_{3+\delta}$	8.4	5.9	3.4	4.5	529.2	513.8
$LaFeO_3$	8.3	6.7	3.1	4.4	529.1	513.7
$LaCoO_3$	7.7	6.0	3.3	4.9	528.6	514.6
$LaNiO_{3-\delta}$	7.5	6.2	4	5.3	528.2	515.0
LSCO20	7.7	6.2	4.4	5.0	528.5	514.9
LSCO50	7.7	6.4	4.6	5.7	528.4	515.1
GBCO	7.3	5.4	3.8	5.4	527.9	515.5
SBCO	7.3	5.5	3.9	5.5	528.1	514.9
PBCO	7.2	5.6	4.1	5.6	527.7	515.9
BSCF	8.5	n/a	5.1	7.0	529.3	514.1
$SrFeO_{3-\delta}$	7.5	n/a	4.3	4.6	528.3	515.3
$CaFeo_{3-\delta}$	8.0	6.1	2.4	3.8	529.1	512.6
$Sr_{0.5}Ca_{0.5}Feo_{3-\delta}$	7.8	n/a	2.5	4.0	528.7	513.9

NB: O 2*p* non-bonding band position (peak B, **Fig. 2**) relative to vacuum, eV.

IE: Ionization energy (peak C, **Fig. 2**) relative to vacuum, eV. Note that BSCF does not have a clear peak C.

EA: Electron affinity (O K XAS pre-edge peak position, Supplementary **Fig. S2**) relative to vacuum, eV. "Unoccupied TM 3*d* – O 2*p*" in **Fig. 4**.

E_F: Fermi level determined from XPS relative to vacuum, eV.

O 1*s* XPS BE: XPS binding energy, eV.

O KLL KE: Auger kinetic energy, eV.

Table S4 | Summary of parameters illustrated in Fig. 4. Oxide abbreviations: $La_{0.8}Sr_{0.2}CoO_{3-\delta}$ (LSCO20), $La_{0.5}Sr_{0.5}CoO_{3-\delta}$ (LSCO50), $GdBaCo_2O_{5+\delta}$ (GBCO), $SmBaCo_2O_{5+\delta}$ (SBCO), $PrBaCo_2O_{5+\delta}$ (PBCO), $Ba_{0.5}Sr_{0.5}Co_{0.8}Fe_{0.2}O_{3-\delta}$ (BSCF). The OER activity (log-current-density at 1.6 V vs. RHE), spectroscopically determined energy barriers (charge-transfer energy, electron transfer barrier, hydroxide affinity), and physiochemical properties (vacancy formation energy,[29-31] Tafel slope of the OER, and pH of zero charge[37]). * denotes literature values for Sr contents *x* slightly different than the ones used here (Δx = 0.1).

Oxide	**log |*i*| (mA/cm^2_{ox} @ 1.6 V vs. RHE)**	**charge-transfer energy (eV)**	**electron transfer (eV)**	**hydroxide affinity (eV)**	**vacancy formation energy (eV)**	**Tafel slope (mV/decade)**	**pH of zero charge**
$LaCrO_3$	−1.07	7.1	4.6	−0.2	--	164	--
$LaMnO_{3+\delta}$	−0.57	5.0	1.1	0.0	4.3	113	7.0
$LaFeO_3$	−0.71	5.2	1.4	−0.1	5.1	95	--
$LaCoO_3$	−0.53	4.4	1.2	0.4	2.1	71	6.7
$LaNiO_{3-\delta}$	−0.07	2.2	0.0	0.8	--	70	8.9
LSCO20	−0.15	3.3	0.1	0.5	1.5	58	7.2*
LSCO50	0.64	2.0	0.0	1.1	0.7	69	8.2*
GBCO	0.39	1.9	0.0	0.9	0.9	60	--
SBCO	0.50	1.8	0.0	1.0	--	60	--
PBCO	0.86	1.6	0.0	1.1	0.8	70	--
BSCF	--	1.6	--	--	--	--	--

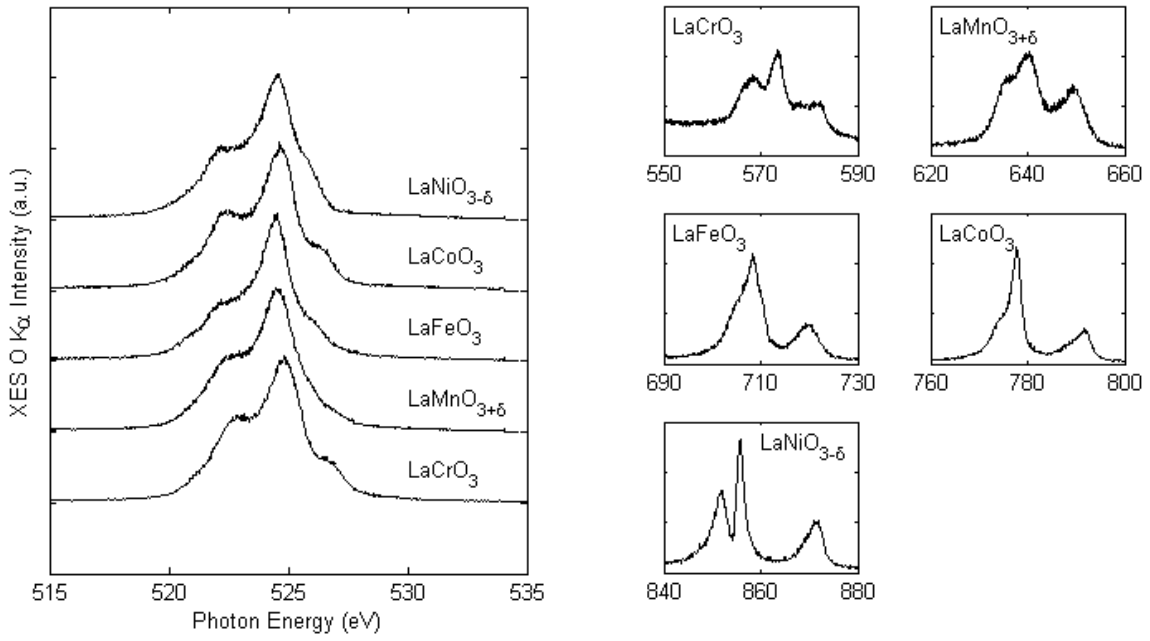
XES O Kα Intensity (a.u.)
LaNiO3-δ
LaCoO3
LaFeO3
LaMnO3+δ
LaCrO3
515
520
525
530
535
Photon Energy (eV)
LaCrO3
550
570
590
LaMnO3+δ
620
640
660
LaFeO3
690
710
730
LaCoO3
760
780
800
LaNiO3-δ
840
860
880

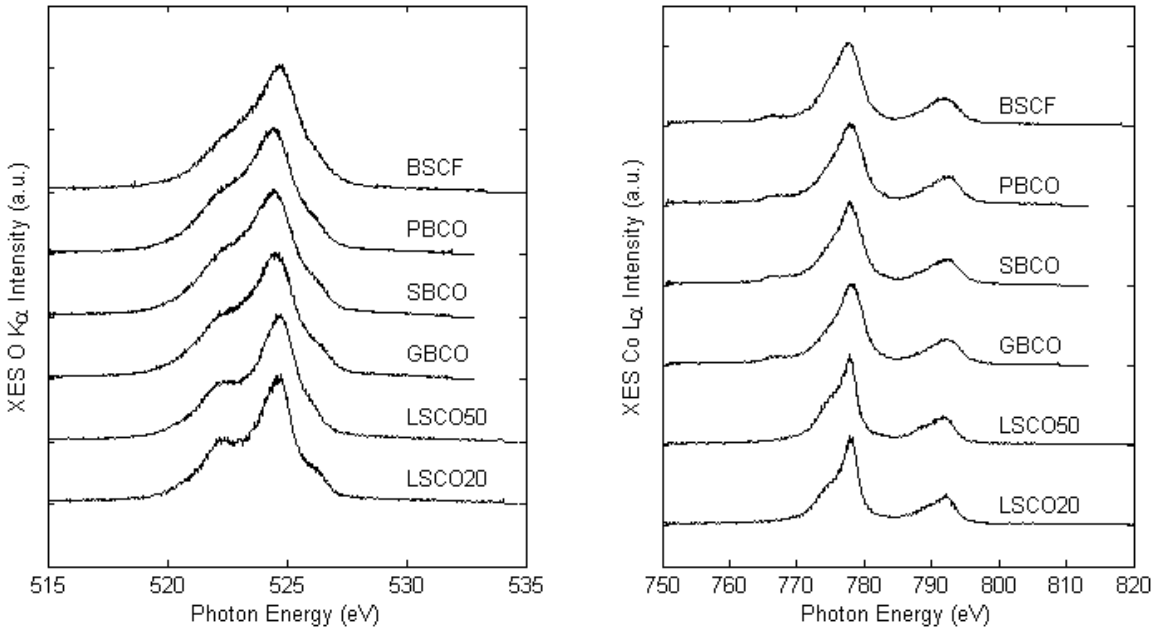
XES O Kα Intensity (a.u.)
BSCF
PBCO
SBCO
GBCO
LSCO50
LSCO20
515
520
525
530
535
Photon Energy (eV)
XES Co Lα Intensity (a.u.)
BSCF
PBCO
SBCO
GBCO
LSCO50
LSCO20
750
760
770
780
790
800
810
820
Photon Energy (eV)

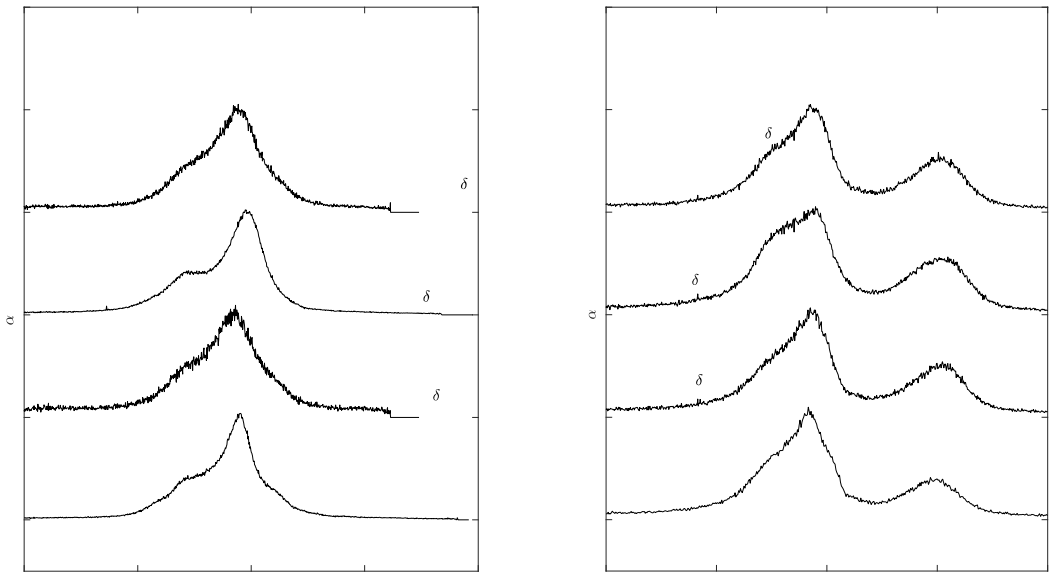

Fig. S1 | Raw XES spectra of all the oxides examined in this work. Oxide abbreviations: $La_{0.8}Sr_{0.2}CoO_{3-\delta}$ (LSCO20), $La_{0.5}Sr_{0.5}CoO_{3-\delta}$ (LSCO50), $GdBaCo_2O_{5+\delta}$ (GBCO), $SmBaCo_2O_{5+\delta}$ (SBCO), $PrBaCo_2O_{5+\delta}$ (PBCO), $Ba_{0.5}Sr_{0.5}Co_{0.8}Fe_{0.2}O_{3-\delta}$ (BSCF). The data for LaMO_3 (M = Cr, Mn, Fe, Co, Ni) were reported previously.[1] The data for LSCO20, LSCO50, GBCO, SBCO, PBCO, BSCF, $SrFeO_{3-\delta}$, $CaFeO_{3-\delta}$, and $Sr_{0.5}Ca_{0.5}FeO_{3-\delta}$ are reported here for the first time.

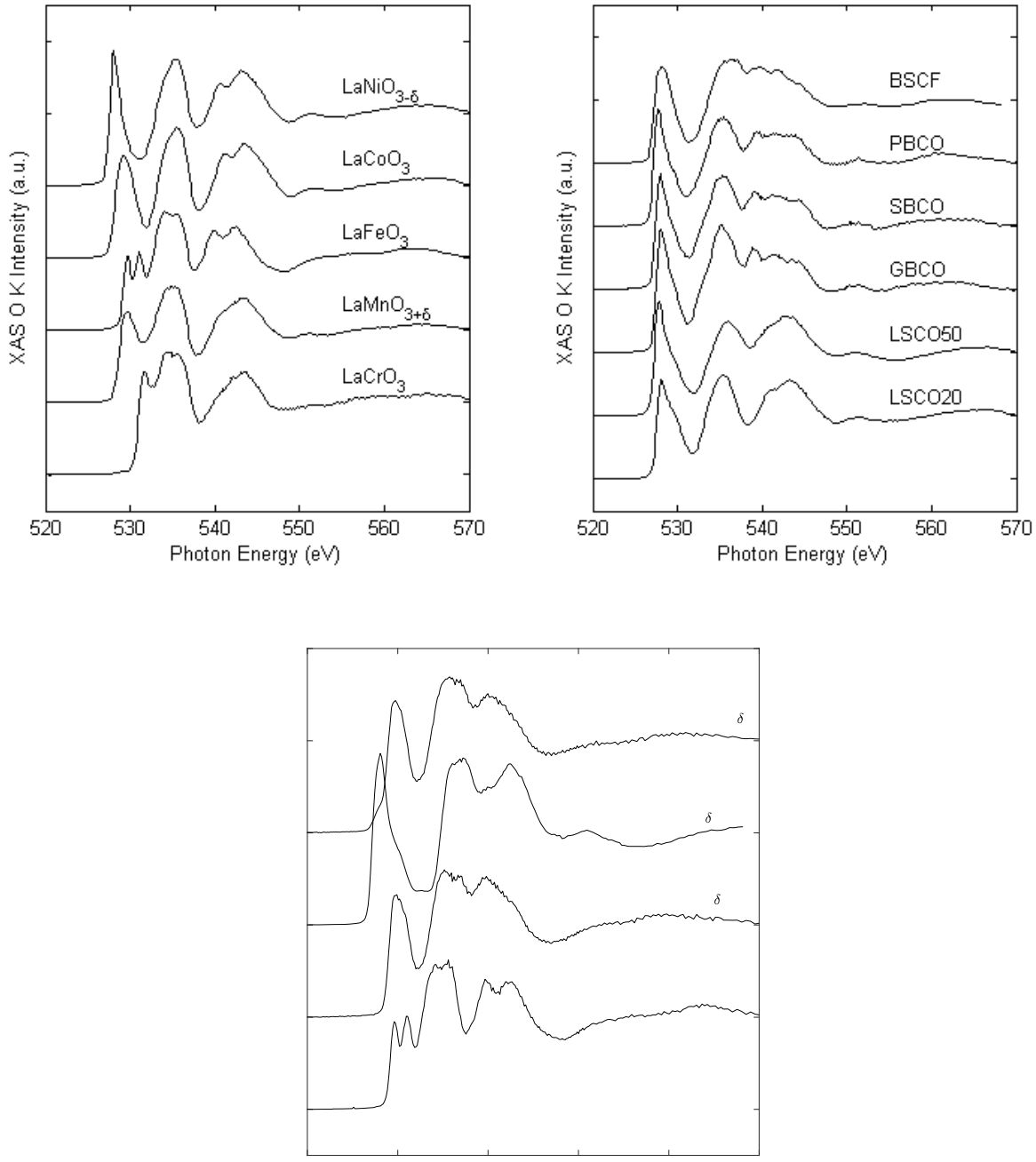

Fig. S2 | Raw O K XAS spectra (total fluorescence yield) of all the oxides in this work. Oxide abbreviations: $La_{0.8}Sr_{0.2}CoO_{3-\delta}$ (LSCO20), $La_{0.5}Sr_{0.5}CoO_{3-\delta}$ (LSCO50), $GdBaCo_2O_{5+\delta}$ (GBCO), $SmBaCo_2O_{5+\delta}$ (SBCO), $PrBaCo_2O_{5+\delta}$ (PBCO), $Ba_{0.5}Sr_{0.5}Co_{0.8}Fe_{0.2}O_{3-\delta}$ (BSCF). The data for LaMO$_3$ (M = Cr, Mn, Fe, Co, Ni) were reported previously.[1] The data for LSCO20, LSCO50, GBCO, SBCO, PBCO, BSCF, $SrFeO_{3-\delta}$, $CaFeO_{3-\delta}$, and $Sr_{0.5}Ca_{0.5}FeO_{3-\delta}$ are reported here for the first time.

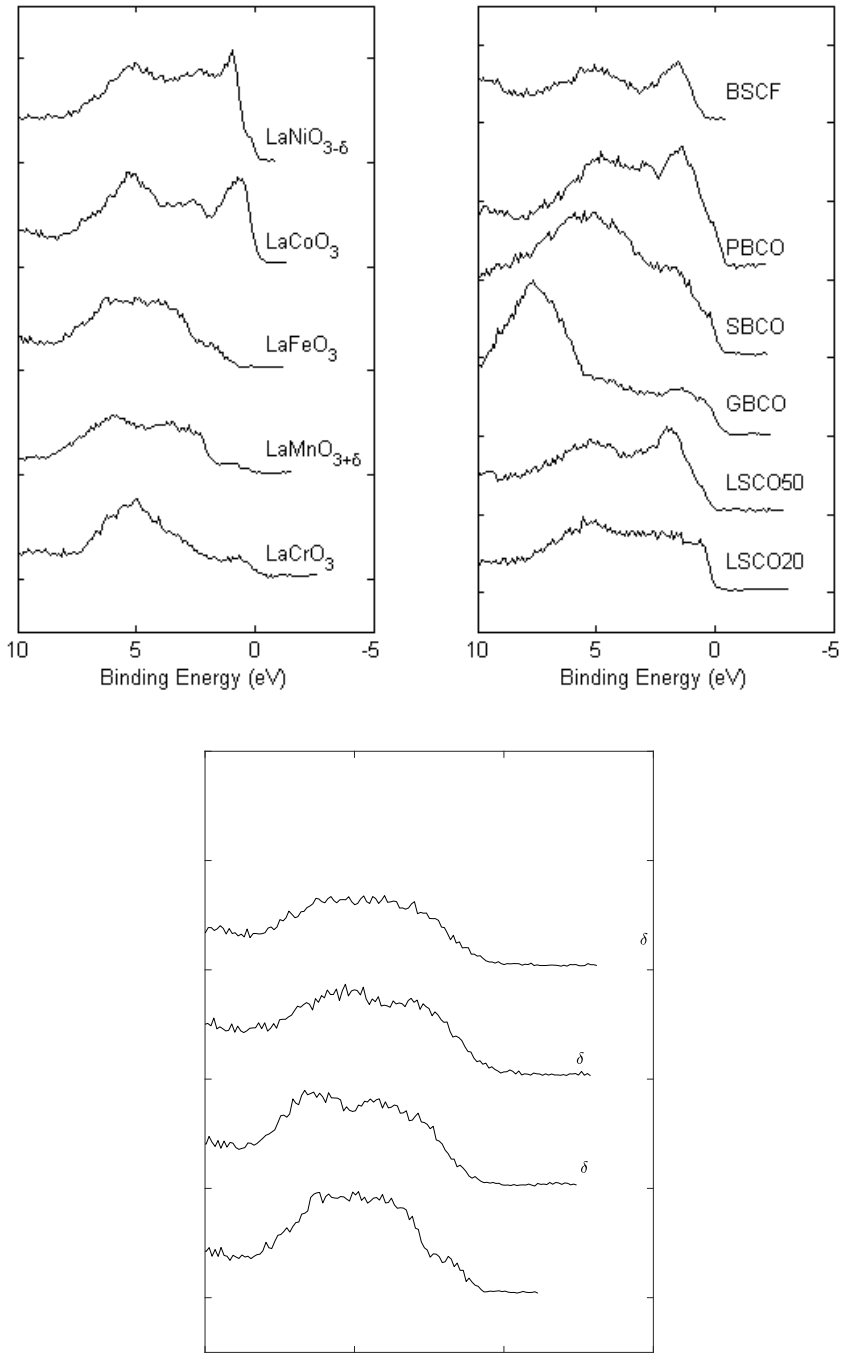

Fig. S3 | Raw valence band XPS spectra (Al Kα source) of all the oxides in this work. Oxide abbreviations: $La_{0.8}Sr_{0.2}CoO_{3-\delta}$ (LSCO20), $La_{0.5}Sr_{0.5}CoO_{3-\delta}$ (LSCO50), $GdBaCo_2O_{5+\delta}$ (GBCO), $SmBaCo_2O_{5+\delta}$ (SBCO), $PrBaCo_2O_{5+\delta}$ (PBCO), $Ba_{0.5}Sr_{0.5}Co_{0.8}Fe_{0.2}O_{3-\delta}$ (BSCF). The data for LaMO_3 (M = Cr, Mn, Fe, Co, Ni) were reported previously.[1] The data for LSCO20, LSCO50, GBCO, SBCO, PBCO, BSCF, $SrFeO_{3-\delta}$, $CaFeO_{3-\delta}$, and $Sr_{0.5}Ca_{0.5}FeO_{3-\delta}$ are reported here for the first time. Spectra aligned to the sample Fermi level using the adventitious carbon peak of the C 1s spectra (E_B = 284.8 eV) for semiconducting samples (LaCrO3, $LaMnO_{3+\delta}$, $LaFeO_3$, $LaCoO_3$, LSCO20, BSCF) and the Fermi edge using a Heaviside function for conducting samples ($LaNiO_{3-\delta}$, LSCO50, GBCO, SBCO, PBCO).

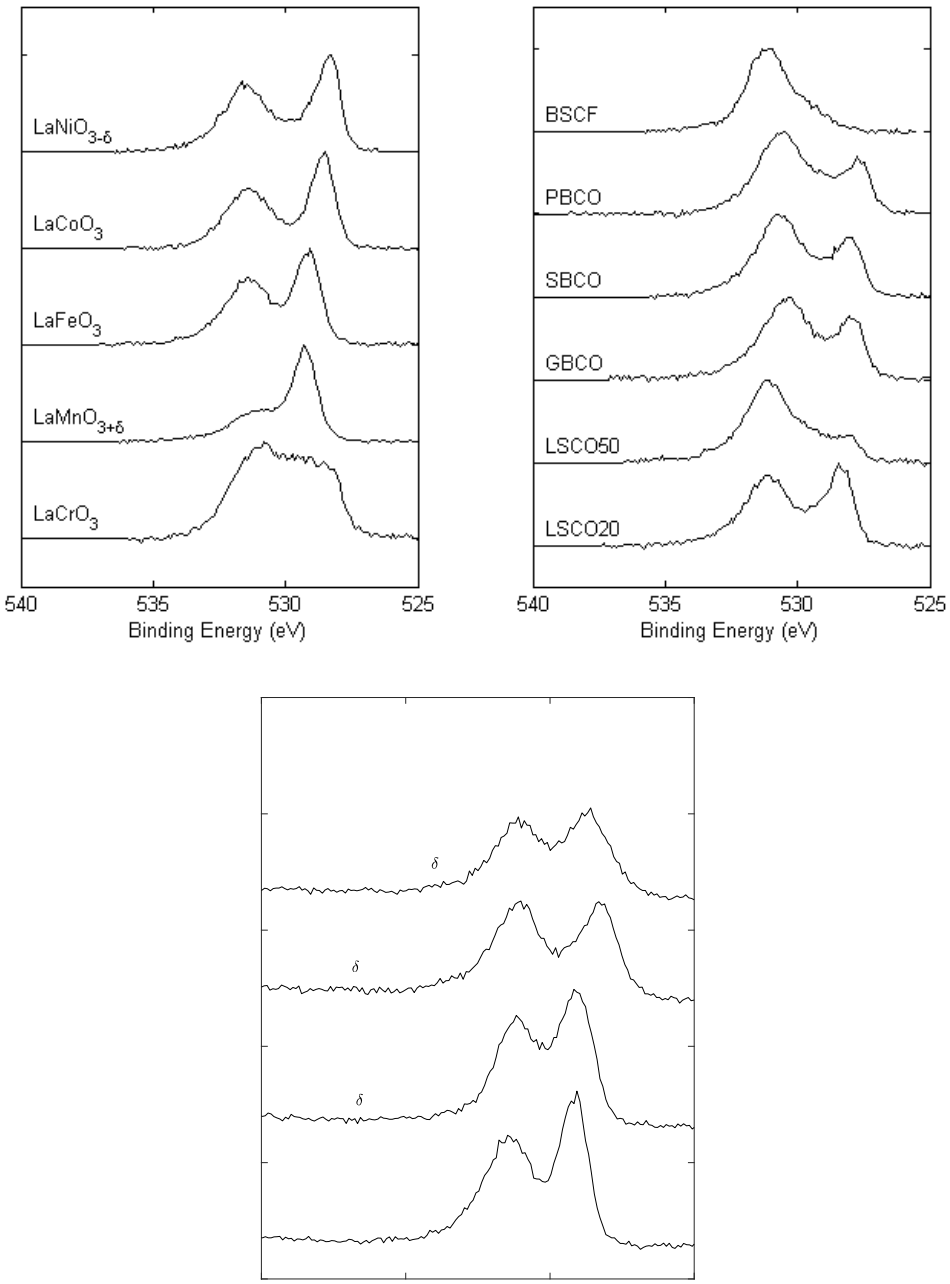

Fig. S4 | Background-subtracted O 1*s* XPS spectra (Al K*α* source) of all the oxides in this work. Oxide abbreviations: $La_{0.8}Sr_{0.2}CoO_{3-\delta}$ (LSCO20), $La_{0.5}Sr_{0.5}CoO_{3-\delta}$ (LSCO50), $GdBaCo_2O_{5+\delta}$ (GBCO), $SmBaCo_2O_{5+\delta}$ (SBCO), $PrBaCo_2O_{5+\delta}$ (PBCO), $Ba_{0.5}Sr_{0.5}Co_{0.8}Fe_{0.2}O_{3-\delta}$ (BSCF). Spectra aligned to the sample Fermi level using the adventitious carbon peak of the C 1s spectra (E_B = 284.8 eV) for semiconducting samples (LaCrO3, $LaMnO_{3+\delta}$, $LaFeO_3$, $LaCoO_3$, LSCO20, BSCF) and the Fermi edge using a Heaviside function for conducting samples ($LaNiO_{3-\delta}$, LSCO50, GBCO, SBCO, PBCO). For each oxide, the lowest energy O 1s peak (associated with the bulk oxide) was fit to a Gaussian-Lorentzian peak (30% Lorentzian) after a Shirley-type background subtraction to extract the binding energy (CasaXPS).

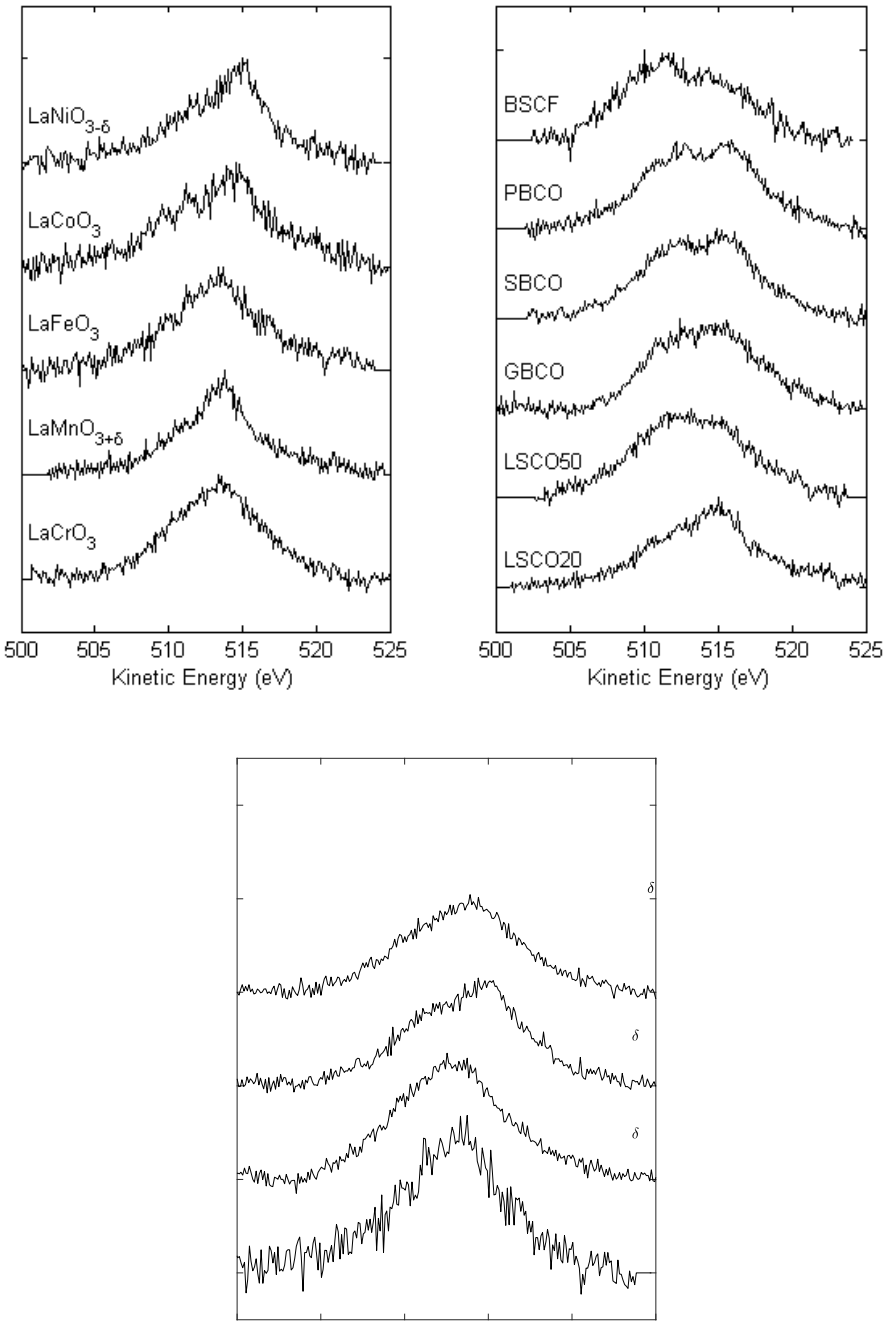

Fig. S5 | Background-subtracted O KLL XPS spectra (Al K*α* source) of all the oxides in this work. Oxide abbreviations: $La_{0.8}Sr_{0.2}CoO_{3-\delta}$ (LSCO20), $La_{0.5}Sr_{0.5}CoO_{3-\delta}$ (LSCO50), $GdBaCo_2O_{5+\delta}$ (GBCO), $SmBaCo_2O_{5+\delta}$ (SBCO), $PrBaCo_2O_{5+\delta}$ (PBCO), $Ba_{0.5}Sr_{0.5}Co_{0.8}Fe_{0.2}O_{3-\delta}$ (BSCF). Spectra aligned to the sample Fermi level using the adventitious carbon peak of the C 1s spectra (E_B = 284.8 eV) for semiconducting samples (LaCrO3, $LaMnO_{3+\delta}$, $LaFeO_3$, $LaCoO_3$, LSCO20, BSCF) and the Fermi edge using a Heaviside function for conducting samples ($LaNiO_{3-\delta}$, LSCO50, GBCO, SBCO, PBCO). A regional maximum (CasaXPS) was used to obtain the position of the main O KLL Auger transition kinetic energy, except for those of LSCO50 and BSCF, in which the main O KLL transition differs – instead, the high-energy transition was fit in the same manner as the O 1s spectra.

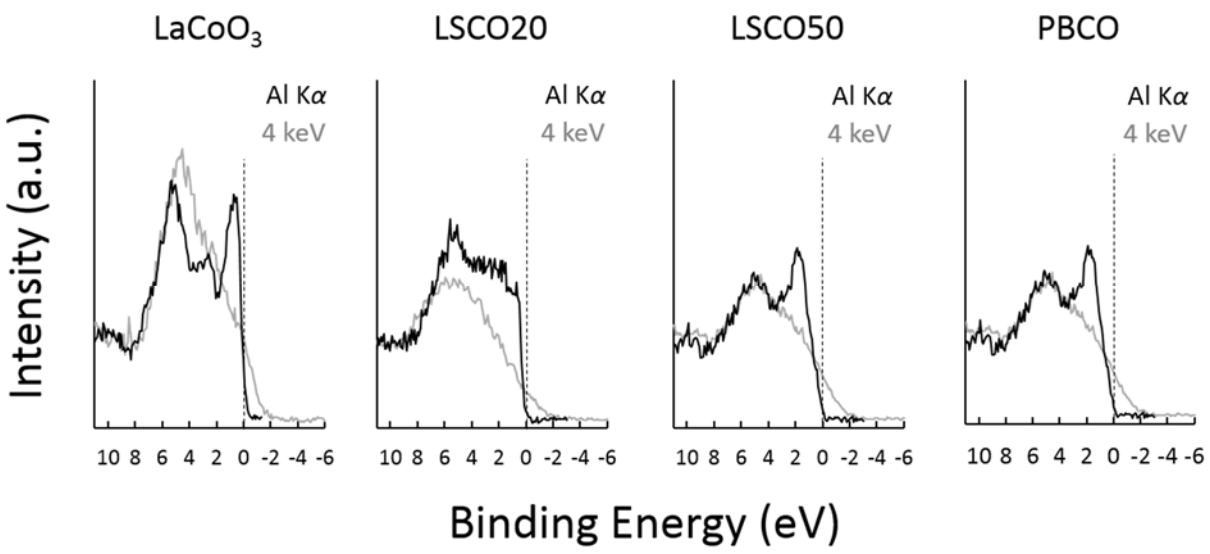

Fig. S6 | Comparison of valence band measurements performed using an Al K*α* source (black) and 4 keV incident energy on Beamline 9.3.1 at the Advanced Light Source (gray). Oxide abbreviations: $La_{0.8}Sr_{0.2}CoO_{3-\delta}$ (LSCO20), $La_{0.5}Sr_{0.5}CoO_{3-\delta}$ (LSCO50), $PrBaCo_2O_{5+\delta}$ (PBCO). Dashed line illustrates the experimental Fermi level.

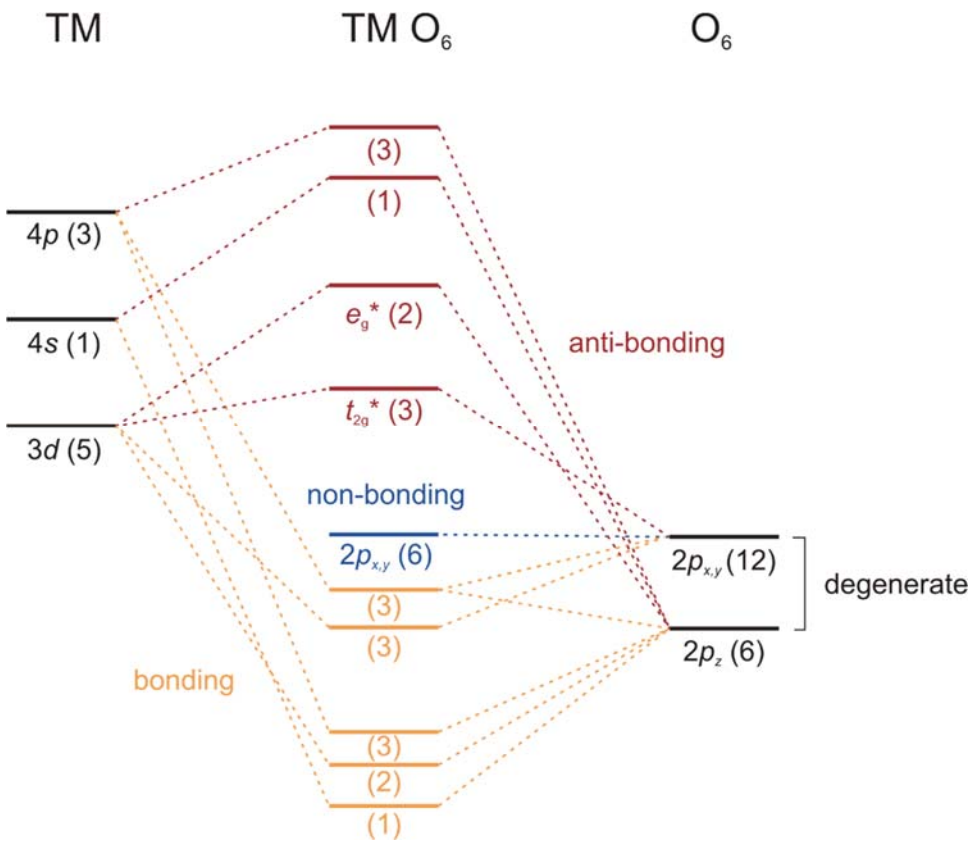

Fig. S7 | Molecular orbital diagram of a transition metal atom in ideal octahedral coordination with six oxygen atoms.[38, 39] The transition metal and oxygen atomic orbitals are shown on the left and right, respectively. The degeneracies of all atomic and molecular orbitals are shown in parentheses. The molecular orbitals can be categorized into anti-bonding (red), non-bonding (blue), and bonding (orange) states. Distortion of the octahedral environment results in further state splitting.

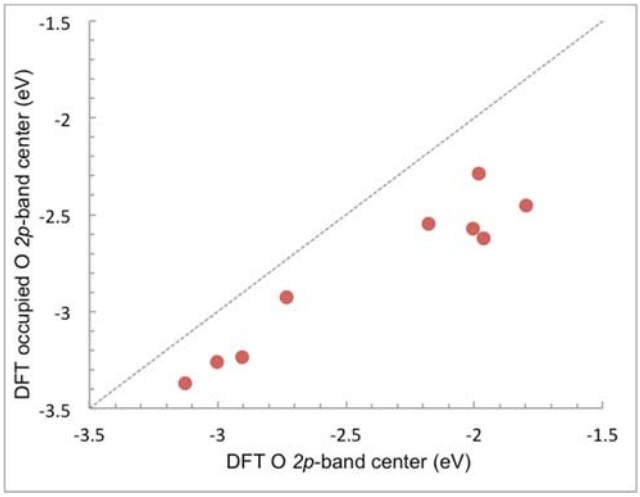

Fig. S8 | Correlation between the O 2*p*-band center computed from only the occupied oxygen PDOS and the O 2*p*-band center computed from the full oxygen PDOS (occupied and unoccupied). A nearly 1:1 correspondence exists for the O 2p-band center computed from both occupied and unoccupied versus only the occupied.

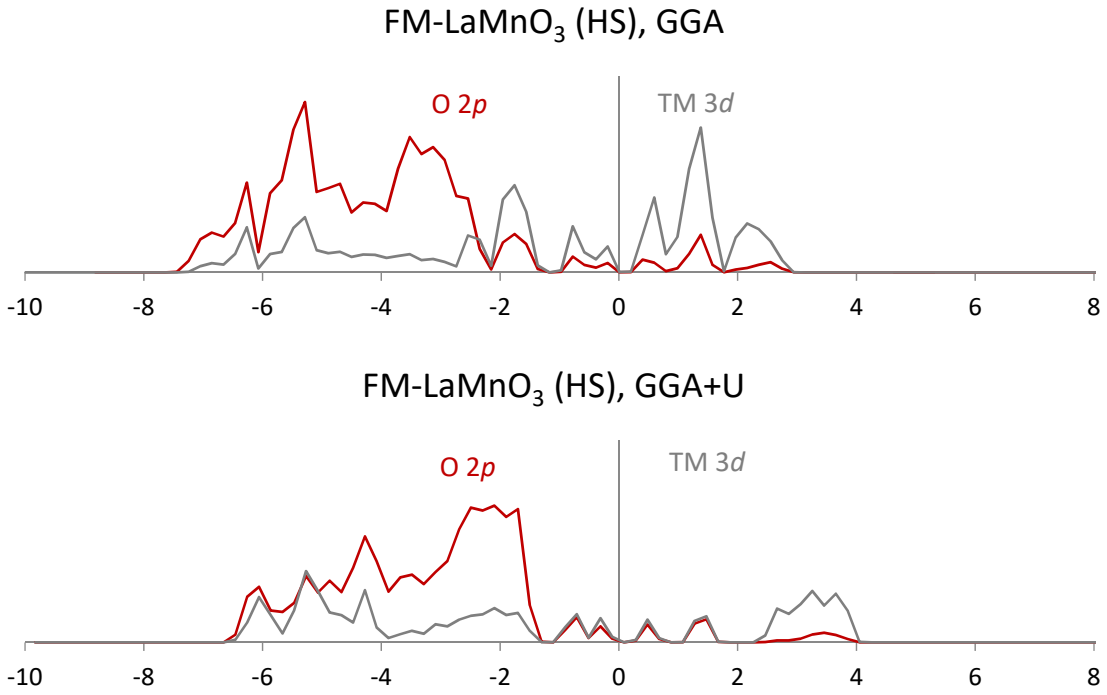

Fig. S9 | DFT calculations of $LaMnO_3$ without and with U_{eff} = 4.0 eV. The inclusion of U_{eff} causes the TM 3*d* states to split more drastically, shifting the calculated O 2*p*-band center from −3.9 eV to −3.1 eV. The experimental O 2*p*-band center is −3.4 eV, suggesting values of U_{eff} used in this study may overcompensate for electron correlations.

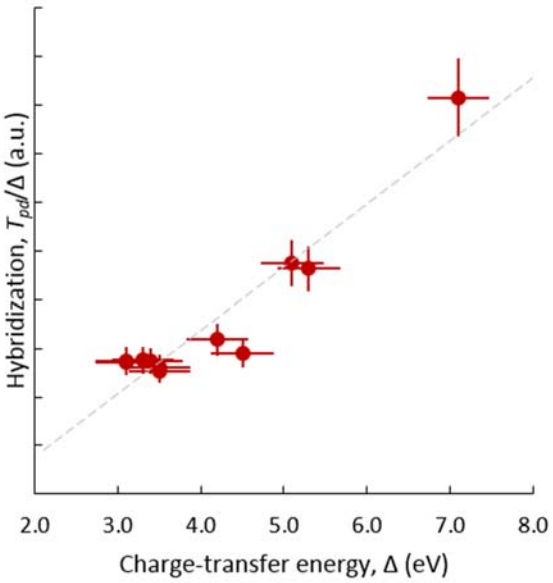

Fig. S10 | Correlation between metal-oxygen hybridization and charge-transfer energy. Error bars in the charge-transfer energy were obtained using the uncertainty in XES and XAS feature positions, as described previously.[1] Error bars in the metal-oxygen hybridization are estimated to be 10%.[11]

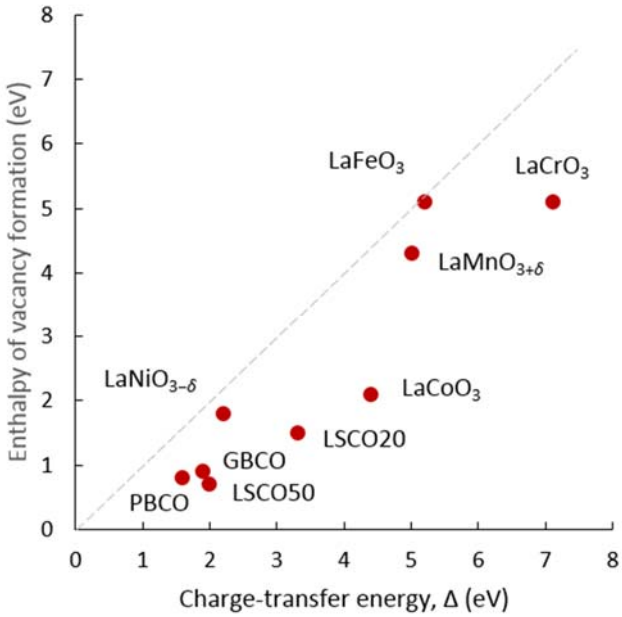

Fig. S11 | Correlation between enthalpy of oxygen vacancy formation[29-33] and charge-transfer energy.

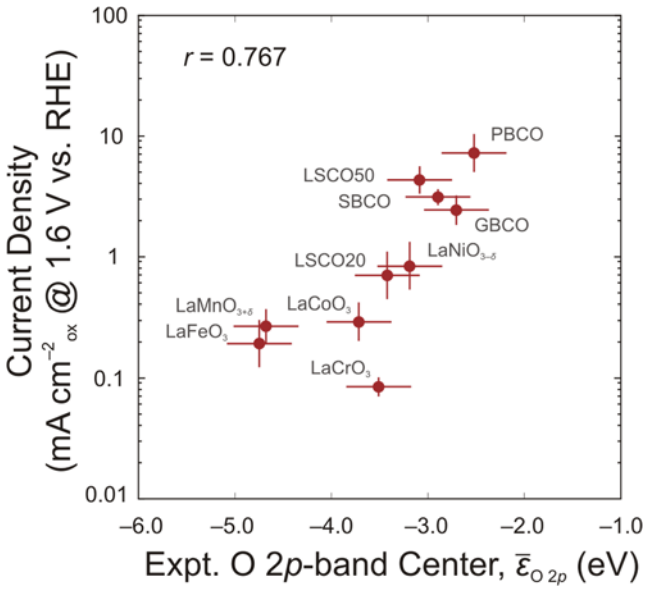

Fig. S12 | Correlation between the OER kinetic current at 1.6 V vs. RHE and the experimental O 2*p*-band center. Oxide abbreviations: $La_{0.8}Sr_{0.2}CoO_{3-\delta}$ (LSCO20), $La_{0.5}Sr_{0.5}CoO_{3-\delta}$ (LSCO50), $GdBaCo_2O_{5+\delta}$ (GBCO), $SmBaCo_2O_{5+\delta}$ (SBCO), $PrBaCo_2O_{5+\delta}$ (PBCO). Error bars in the experimental O 2*p*-band center were estimated as the error in XPS calibration (0.5 eV, see Supplementary Methods for details). Pearson correlation coefficient is shown. Statistical comparisons of the correlation coefficient with that of the charge-transfer energy are shown in **Figs. S14**, **S15**.

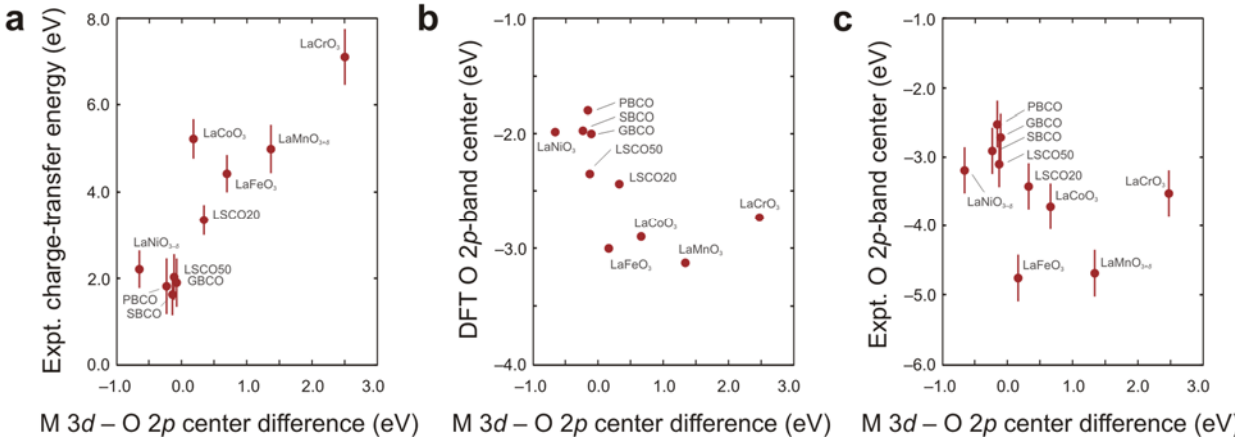

Figure S13 | Relationships between the O 2*p*-band center, charge-transfer energy, and M 3*d* and O 2*p* band positions. Oxide abbreviations: $La_{0.8}Sr_{0.2}CoO_{3-\delta}$ (LSCO20), $La_{0.5}Sr_{0.5}CoO_{3-\delta}$ (LSCO50), $GdBaCo_2O_{5+\delta}$ (GBCO), $SmBaCo_2O_{5+\delta}$ (SBCO), $PrBaCo_2O_{5+\delta}$ (PBCO). **a,** Relationship between the experimentally measured charge-transfer energy and the DFT-computed M 3*d*-band and O 2*p*-band center difference. **b,** Relationship between the DFT-computed O 2*p*-band center vs. the Fermi level and the DFT-computed M 3*d*-band and O 2*p*-band center difference. **c,** Relationship between the experimentally measured O 2*p*-band center vs. the Fermi level and the DFT-computed M 3*d*-band and O 2*p*-band center difference. Error bars in the charge-transfer energy were obtained using the uncertainty in XES and XAS feature positions, as described previously.[1] Error bars in the

experimental O 2*p*-band center were estimated as the error in XPS calibration (0.5 eV, see Supplementary Information for details).

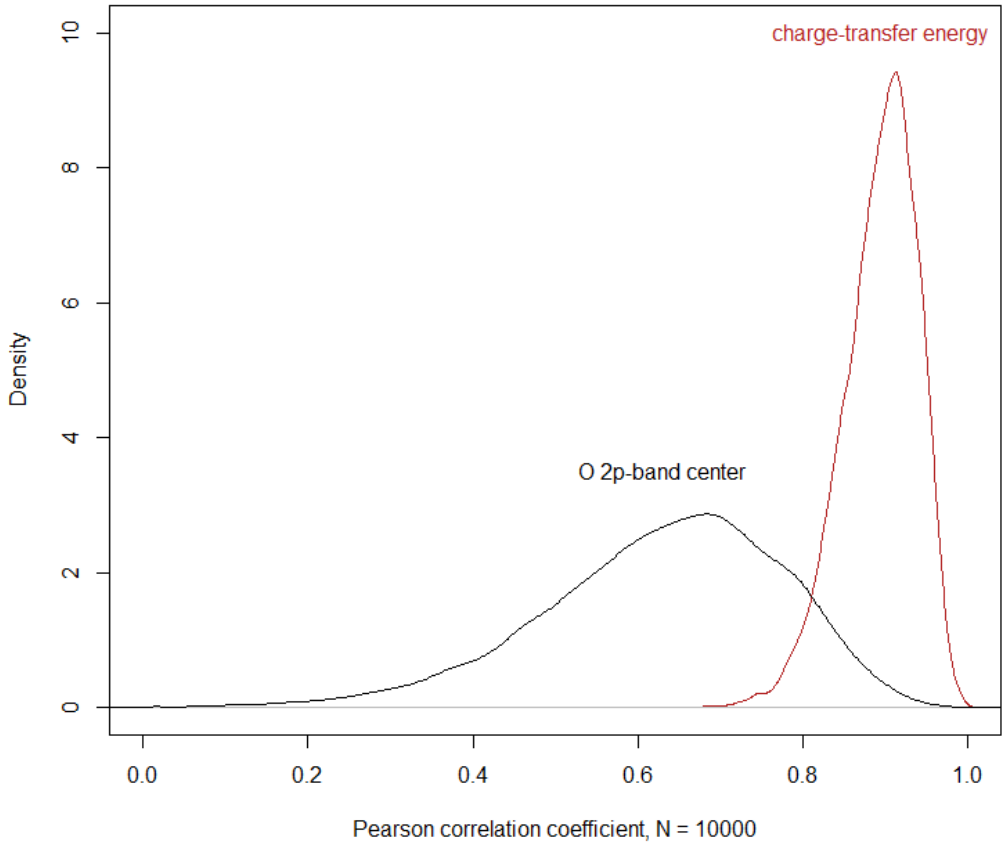

Fig. S14. | Probability density distributions of the Pearson correlation coefficients for the charge-transfer energy and O 2*p*-band center as OER activity descriptors. Correlation coefficients were calculated from parametric resampling (10,000 simulations) of the charge-transfer energies, O 2*p*-band centers, and OER activities of oxides based on their respective experimental errors. Given these distributions, the probability of superiority for the charge-transfer energy (likelihood that the charge-transfer energy has a higher correlation for a random pairwise outcome) is 98%. The Cohen's *d* effect size is 2.48, which indicates a sizable difference between the performances of the two descriptors.

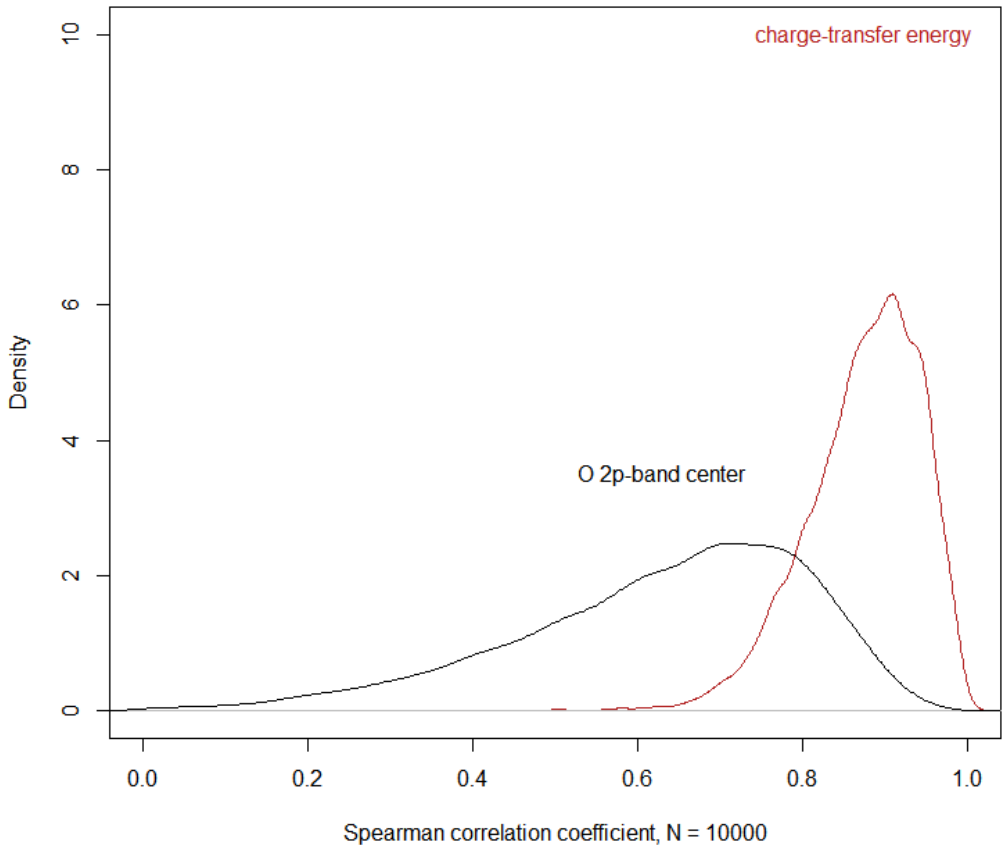

Fig. S15 | Probability density distributions of the Spearman correlation coefficients for the charge-transfer energy and O 2*p*-band center as OER activity descriptors. Correlation coefficients were calculated from parametric resampling (10,000 simulations) of the charge-transfer energies, O 2*p*-band centers, and OER activities of oxides based on their respective experimental errors. The overlap of the distributions increases slightly compared to **Fig. S14**, but the probability of superiority for the charge-transfer energy is still large (92%). The Cohen's *d* effect size is also still large (1.81).

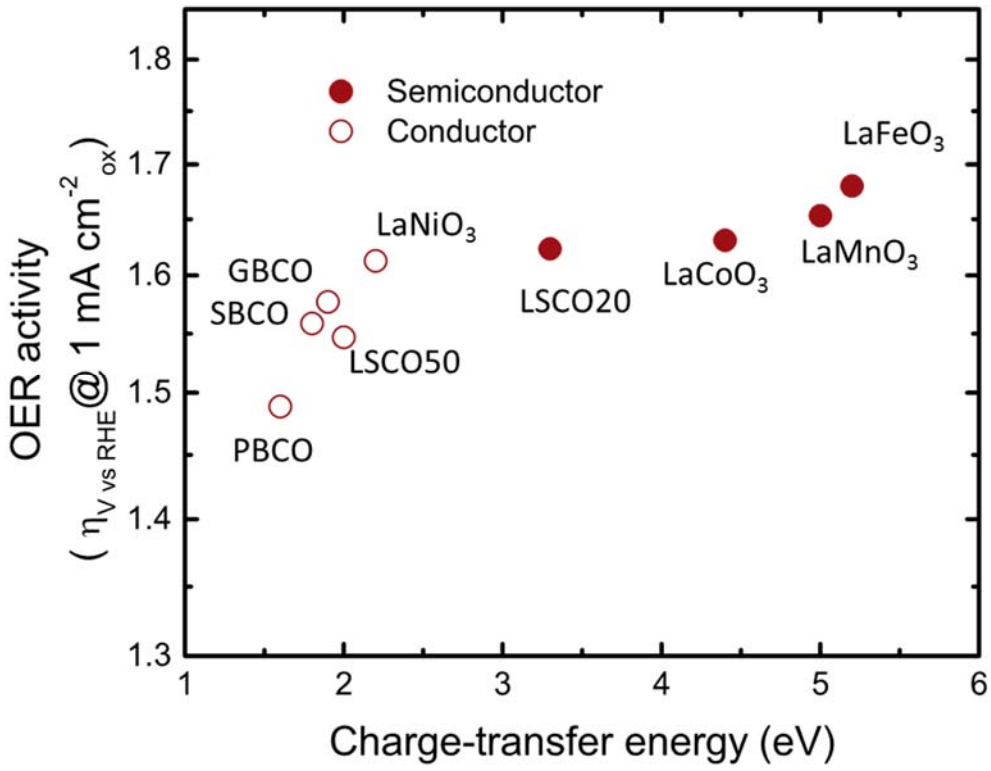

Fig. S16 | Correlation between the OER potential vs. RHE at 1 mA cm^{-2}_{ox} and the experimental charge-transfer energy. Oxide abbreviations: $La_{0.8}Sr_{0.2}CoO_{3-\delta}$ (LSCO20), $La_{0.5}Sr_{0.5}CoO_{3-\delta}$ (LSCO50), $GdBaCo_2O_{5+\delta}$ (GBCO), $SmBaCo_2O_{5+\delta}$ (SBCO), $PrBaCo_2O_{5+\delta}$ (PBCO).

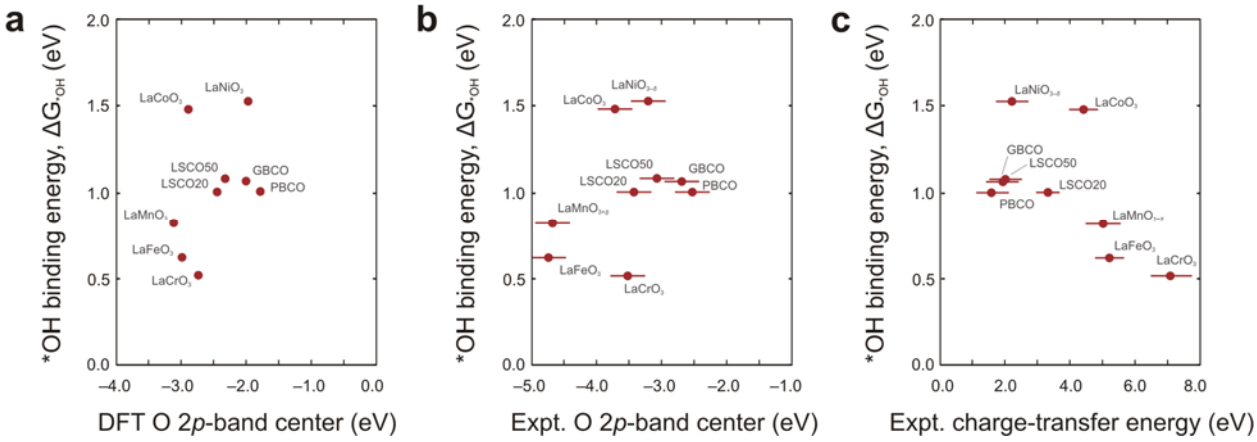

Figure S17 | Relationships between the *OH binding energy,[40, 41] DFT and experimental O 2*p*-band centers, and charge-transfer energy. Oxide abbreviations: $La_{0.8}Sr_{0.2}CoO_{3-\delta}$ (LSCO20), $La_{0.5}Sr_{0.5}CoO_{3-\delta}$ (LSCO50), $GdBaCo_2O_{5+\delta}$ (GBCO), $SmBaCo_2O_{5+\delta}$ (SBCO), $PrBaCo_2O_{5+\delta}$ (PBCO). **a,** Relationship between the DFT-computed *OH adsorbate binding energy on the metal site and the DFT-computed O 2*p*-band center. **b,** Relationship between the DFT-computed *OH adsorbate binding energy on the metal site and the experimental O 2*p*-band center. **c,** Relationship between the DFT-computed *OH adsorbate binding energy on the metal site and the experimental charge-transfer energy. Error bars in the charge-transfer energy were obtained using the uncertainty in XES and XAS feature positions, as described previously.[1] Error bars in the experimental O 2*p*-band center were estimated as the error in XPS calibration (0.5 eV, see Supplementary Information for details).

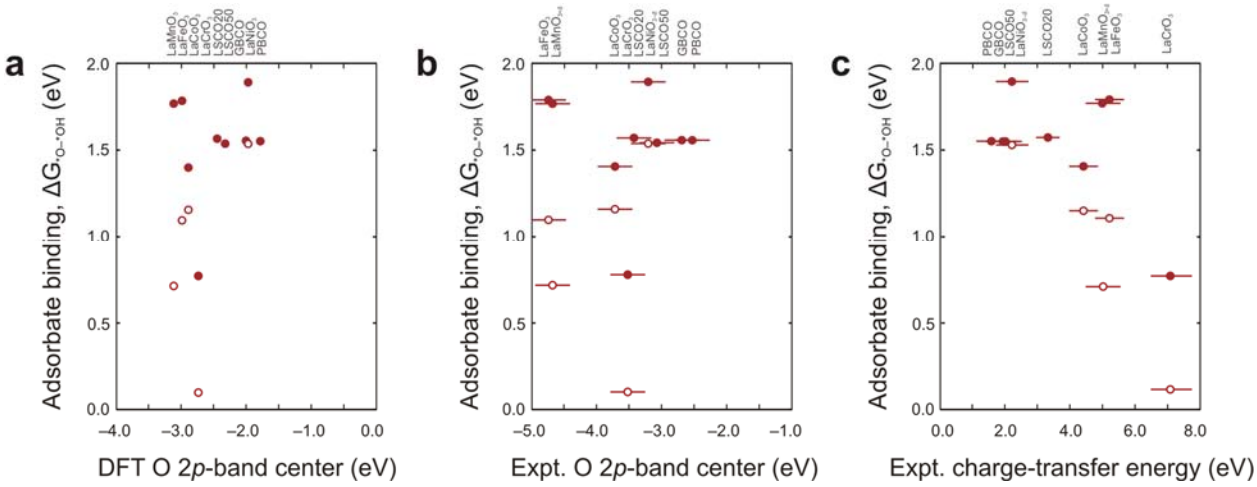

Figure S18 | Relationships between the *O – *OH adsorbate binding descriptor[40, 41] proposed by Man et al.,[41] DFT and experimental O 2*p*-band centers, and charge-transfer energy. Oxide abbreviations: $La_{0.8}Sr_{0.2}CoO_{3-\delta}$ (LSCO20), $La_{0.5}Sr_{0.5}CoO_{3-\delta}$ (LSCO50), $GdBaCo_2O_{5+\delta}$ (GBCO), $SmBaCo_2O_{5+\delta}$ (SBCO), $PrBaCo_2O_{5+\delta}$ (PBCO). **a,** Relationship between the DFT-computed adsorbate binding descriptor on the metal site and the DFT-computed O 2*p*-band center. **b,** Relationship between the DFT-computed adsorbate binding descriptor on the metal site and the experimental O 2*p*-band center. **c,** Relationship between the DFT-computed adsorbate binding descriptor on the metal site and the experimental charge-transfer energy. Error bars in the charge-transfer energy were obtained using the uncertainty in XES and XAS feature positions, as described previously.[1] Error bars in the experimental O 2*p*-band center were estimated as the error in XPS calibration (0.5 eV, see Supplementary Information for details).

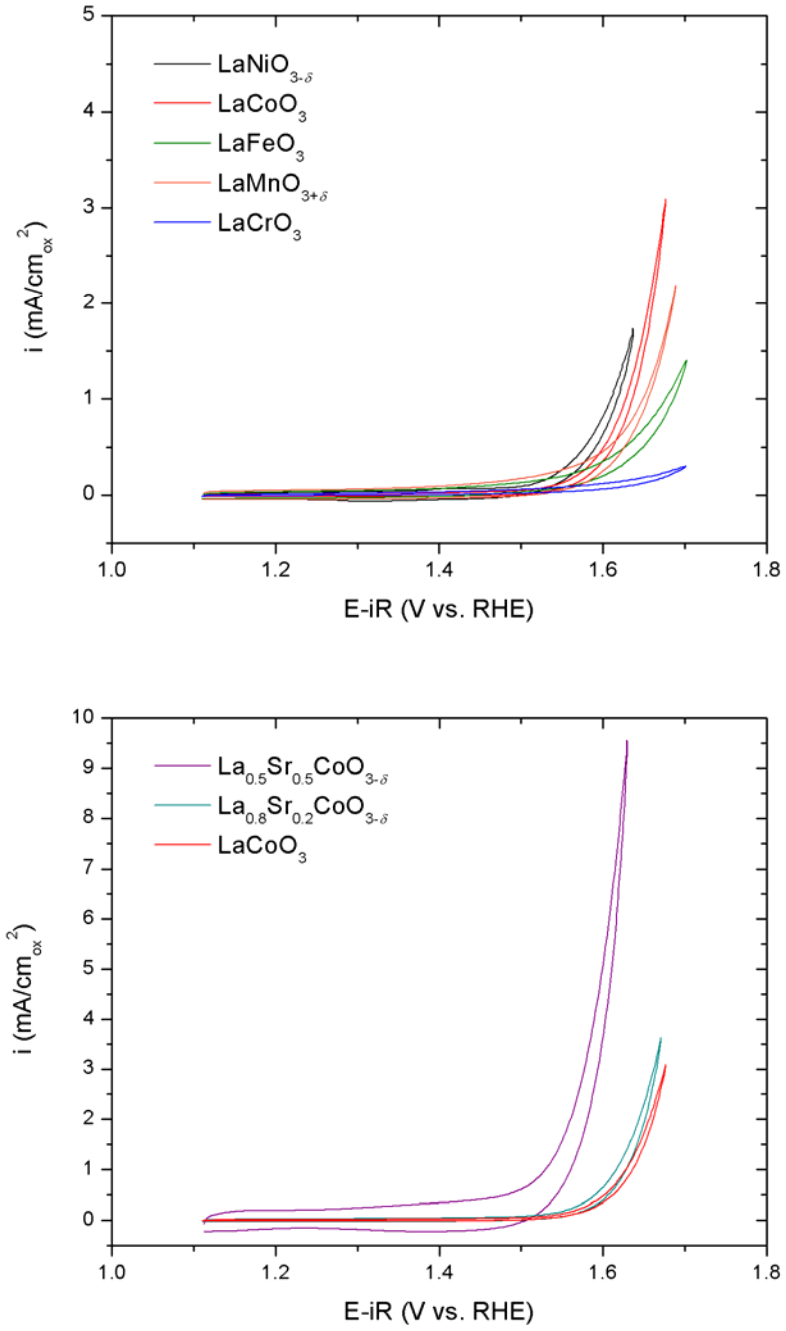

Fig. S19 | Oxygen evolution activities of the studied oxides. Cyclic voltammograms were performed using ink-casted oxides (containing Nafion and acetylene black carbon) with an oxide loading of 0.25 mg/cm$^2_{disk}$ supported on a glassy carbon electrode in O_2-saturated 0.1 M KOH solution, rotating at 1,600 r.p.m. Measurements used a sweep rate of 10 mV/s. Activities were normalized using the BET surface area. Lines correspond to voltammograms from the 2nd cycle.

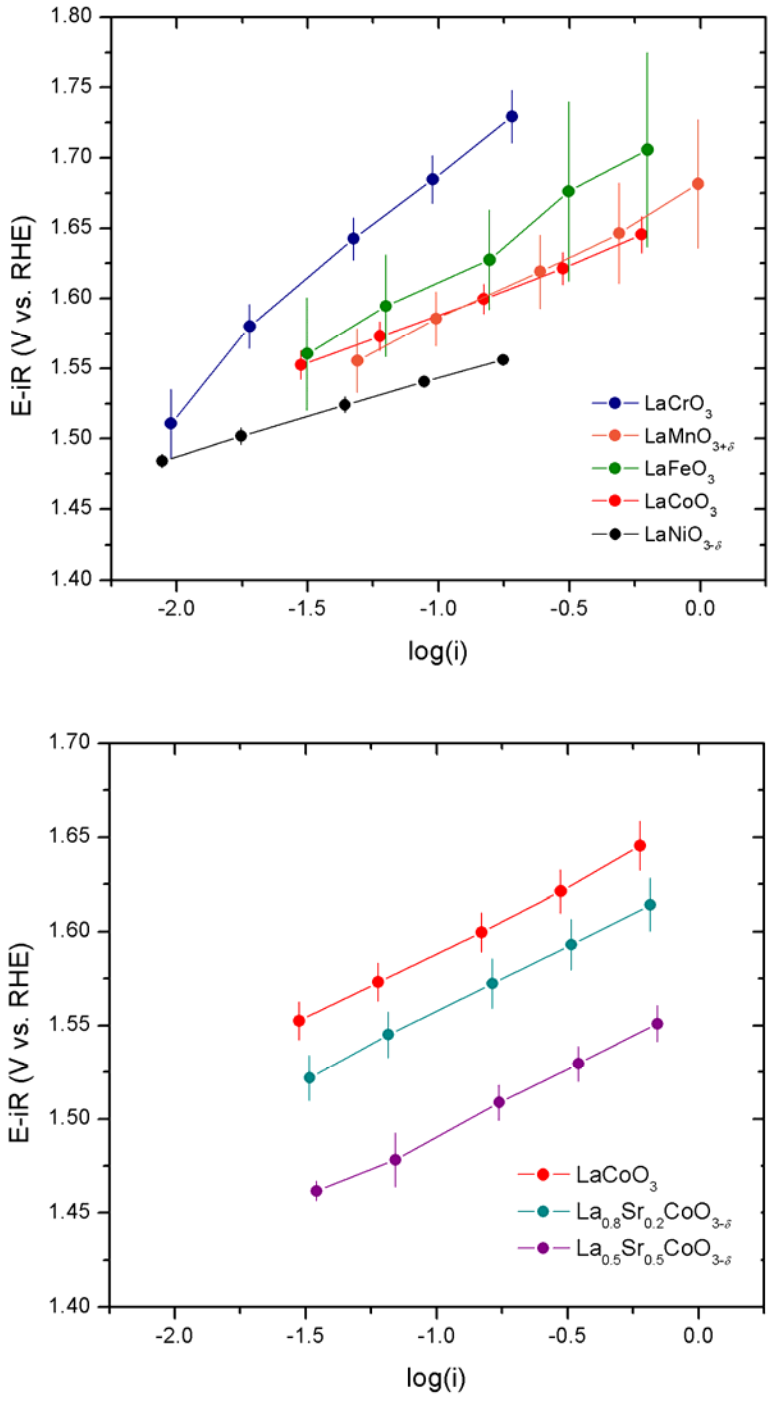

Fig. S20 | Tafel plots from galvanostatic measurements showing E-iR versus log-current-density. Measurements were performed using ink-casted oxides (containing Nafion and acetylene black carbon) with an oxide loading of 0.25 mg/cm^2_{disk} supported on a glassy carbon electrode in O_2-saturated 0.1 M KOH solution, rotating at 1,600

r.p.m. Current density is normalized using the BET surface area. Error bars illustrate 1 s.d. from at least two independent measurements.

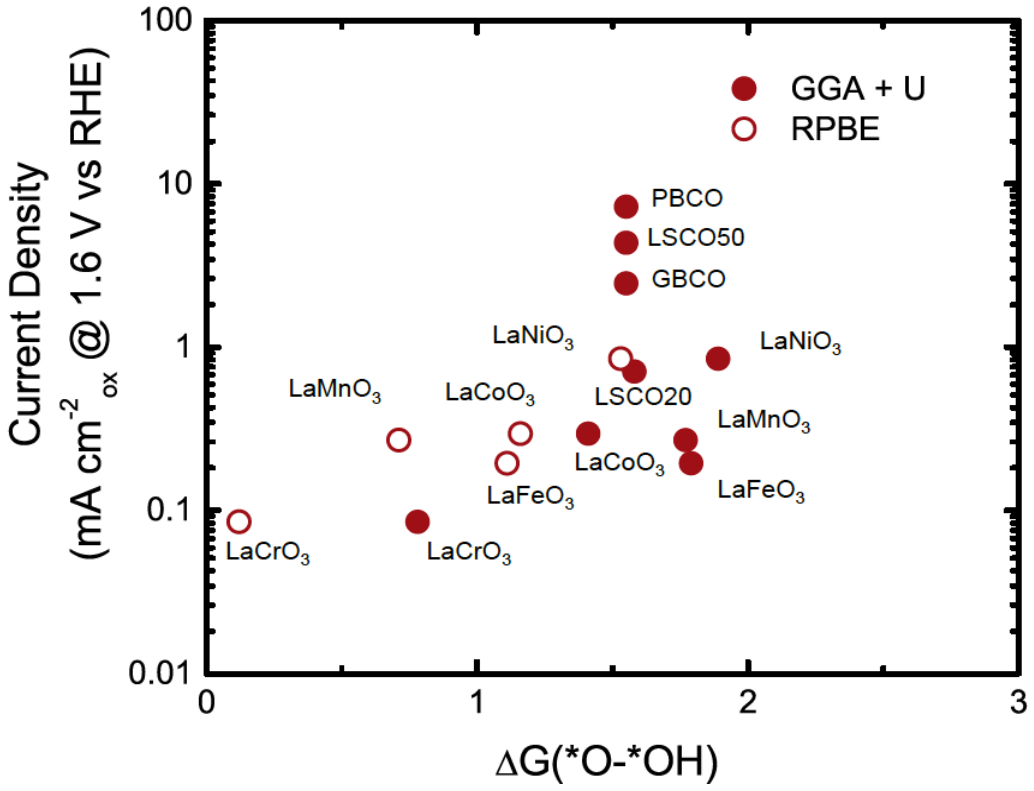

Figure S21 | Relationships between the *O – *OH adsorbate binding descriptor[40, 41] proposed by Man et al.[41] and OER activity. Oxide abbreviations: $La_{0.8}Sr_{0.2}CoO_{3-\delta}$ (LSCO20), $La_{0.5}Sr_{0.5}CoO_{3-\delta}$ (LSCO50), $PrBaCo_2O_{5+\delta}$ (PBCO).

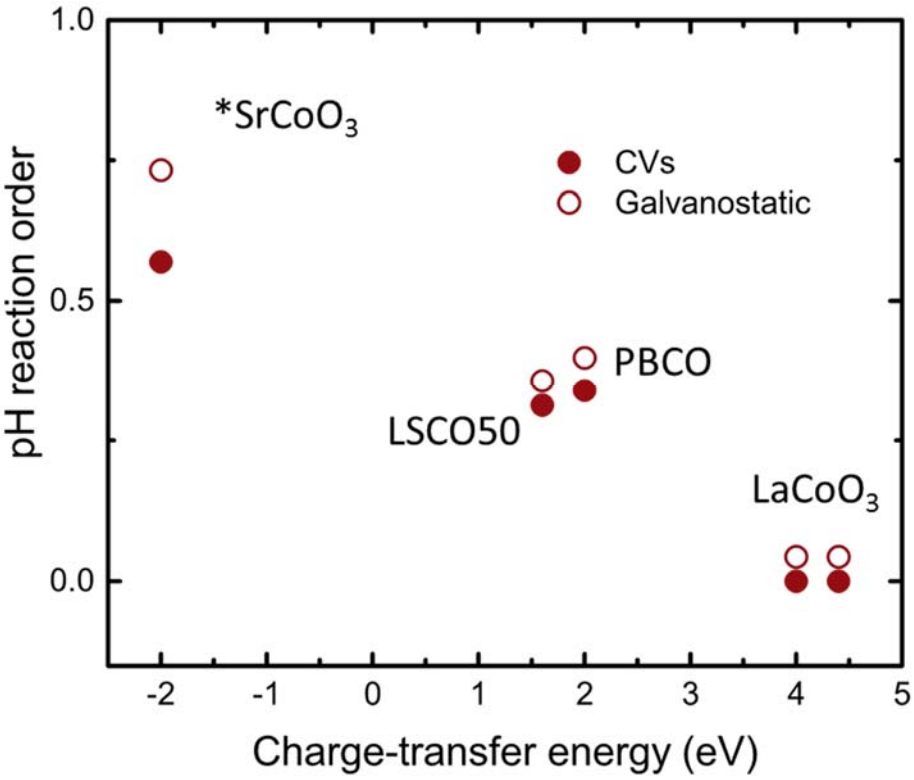

Figure S22 | Relationship between the OER pH reaction order (measured at 1.55 V vs. RHE)[34] and the experimental charge-transfer energy. Oxide abbreviations: $La_{0.5}Sr_{0.5}CoO_{3-\delta}$ (LSCO50), $PrBaCo_2O_{5+\delta}$ (PBCO). The experimental charge-transfer energy of $SrCoO_3$ (*) was previously measured by Abbate et al.[42]

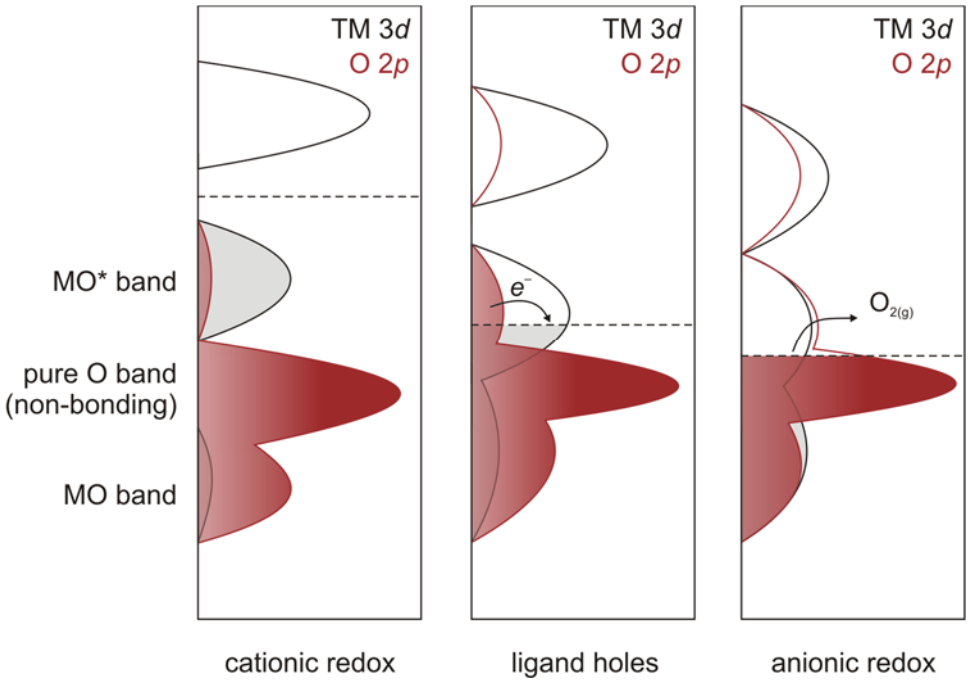

Fig. S23 | Expected transition from cationic redox chemistry to anionic redox chemistry in oxides with different charge-transfer energies. As the charge-transfer energy decreases, the antibonding band becomes depopulated and the Fermi level begins to include electronic states with O 2*p* non-bonding character that promote anionic redox reactions.

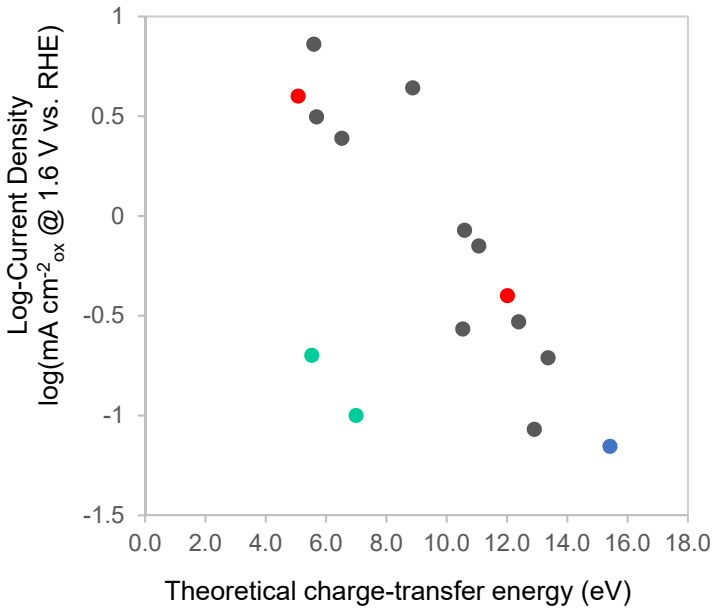

Fig. S24 | Experimental OER activities of different oxide families as a function of theoretical charge-transfer energy. Charge-transfer energies were estimated using the method of Torrance et al. Data points represent perovskite (gray, this work), rutile (green),[43] spinel (blue),[44] and layered (red)[45] oxides.

Supplementary References

1. W. T. Hong, K. A. Stoerzinger, B. Moritz, T. P. Devereaux, W. Yang and Y. Shao-Horn, *J. Phys. Chem. C*, 2015, **119**, 2063-2072.
2. G. Moretti, *J. Electron Spectrosc. Relat. Phenom.*, 1998, **95**, 95-144.
3. C. D. Wagner, L. H. Gale and R. H. Raymond, *Anal. Chem.*, 1979, **51**, 466-482.
4. T. Kida, G. Guan and A. Yoshida, *Chem. Phys. Lett.*, 2003, **371**, 563-567.
5. T. Arima, Y. Tokura and J. Torrance, *Phys. Rev. B*, 1993, **48**, 17006-17009.
6. M. A. Señarís-Rodríguez and J. B. Goodenough, *J. Solid State Chem.*, 1995, **118**, 323-336.
7. B. Rivas-Murias, J. Rivas and M. A. Señarís-Rodríguez, *J. Alloys Compd.*, 2012, **516**, 113-118.
8. T. L. Barr and S. Seal, *J. Vac. Sci. Technol., A*, 1995, **13**, 1239-1246.
9. W. Gries, *Surf. Interface Anal.*, 1996, **24**, 38-50.
10. M. T. Anthony and M. P. Seah, *Surf. Interface Anal.*, 1984, **6**, 107-115.
11. J. Suntivich, W. T. Hong, Y.-L. Lee, J. M. Rondinelli, W. Yang, J. B. Goodenough, B. Dabrowski, J. W. Freeland and Y. Shao-Horn, *J. Phys. Chem. C*, 2014, **118**, 1856-1863.
12. J. B. Goodenough, *Chem. Mater.*, 2014, **26**, 820-829.
13. J. Torrance, P. Lacorre, A. Nazzal, E. Ansaldo and C. Niedermayer, *Phys. Rev. B*, 1992, **45**, 8209-8212.
14. M. H. R. Lankhorst, H. J. M. Bouwmeester and H. Verweij, *J. Am. Ceram. Soc.*, 1997, **80**, 2175-2198.
15. S. Adler, X. Chen and J. Wilson, *J. Catal.*, 2007, **245**, 91-109.
16. P. S. Bagus, F. Illas, G. Pacchioni and F. Parmigiani, *J. Electron Spectrosc. Relat. Phenom.*, 1999, **100**, 215-236.
17. J. B. Goodenough, *J. Appl. Phys.*, 1966, **37**, 1415.
18. H. Kita, N. Henmi, K. Shimazu, H. Hattori and K. Tanabe, *J. Chem. Soc., Faraday Trans. 1*, 1981, **77**, 2451.
19. T. Hiemstra, P. Venema and W. H. Van Riemsdijk, *J. Colloid Interface Sci.*, 1996, **184**, 680-692.
20. M. T. M. Koper, *PCCP*, 2013, **15**, 1399-1407.
21. B. Auer, A. V. Soudackov and S. Hammes-Schiffer, *J. Phys. Chem. B*, 2012, **116**, 7695-7708.
22. C. Contescu, J. Jagiello and J. A. Schwarz, *Langmuir*, 1993, **9**, 1754-1765.
23. P. Cabral do Couto, R. C. Guedes, B. J. Costa Cabral and J. A. Martinho Simões, *J. Chem. Phys.*, 2003, **119**, 7344-7355.
24. B. J. Trzesniewski, O. Diaz-Morales, D. Vermaas, A. Longo, W. Bras, M. T. M. Koper and W. A. Smith, *J. Am. Chem. Soc.*, 2015, **137**, 15112-15121.
25. J. Kim, X. Yin, K. C. Tsao, S. Fang and H. Yang, *J. Am. Chem. Soc.*, 2014, **136**, 14646-14649.
26. A. Nemudry, E. L. Goldberg, M. Aguirre and M. A. Alario-Franco, *Solid State Sci.*, 2002, **4**, 677-690.
27. M. H. R. Lankhorst, H. J. M. Bouwmeester and H. Verweij, *Phys. Rev. Lett.*, 1996, **77**, 2989-2992.
28. J. Zaanen, G. A. Sawatzky and J. Allen, *Phys. Rev. Lett.*, 1985, **55**, 418-421.
29. J. Mizusaki, M. Yoshihiro, S. Yamauchi and K. Fueki, *J. Solid State Chem.*, 1985, **58**, 257-266.
30. J. Mizusaki, Y. Mima, S. Yamauchi and K. Fueki, *J. Solid State Chem.*, 1989, **80**, 102-111.
31. J. Nowotny and M. Rekas, *J. Am. Ceram. Soc.*, 1998, **81**.
32. D. S. Tsvetkov, V. V. Sereda and A. Y. Zuev, *Solid State Ionics*, 2010, **180**, 1620-1625.
33. A. Y. Suntsov, I. A. Leonidov, M. V. Patrakeev and V. L. Kozhevnikov, *J. Solid State Chem.*, 2014, **213**, 93-97.
34. A. Grimaud, O. Diaz-Morales, B. Han, W. T. Hong, Y.-L. Lee, L. Giordano, K. A. Stoerzinger, M. T. Koper and Y. Shao-Horn, *Nat. Chem.*, 2017, **9**, 457-465.
35. J. Rouxel, *Chem. Eur. J.*, 1996, **2**, 1053-1059.

36. X. Rong, J. Parolin and A. M. Kolpak, *ACS Catal.*, 2016, **6**, 1153-1158.
37. J. O. M. Bockris, *J. Electrochem. Soc.*, 1984, **131**, 290.
38. H. Basch, *J. Chem. Phys.*, 1966, **44**, 10.
39. J. E. Huheey, E. A. Keiter and R. L. Keiter, *Inorganic Chemistry: Principles of Structure and Reactivity*, HarperCollins College Publishers, 4th Edition edn., 1993.
40. Y. L. Lee, M. J. Gadre, Y. Shao-Horn and D. Morgan, *PCCP*, 2015, **17**, 21643-21663.
41. I. C. Man, H.-Y. Su, F. Calle-Vallejo, H. A. Hansen, J. I. Martínez, N. G. Inoglu, J. Kitchin, T. F. Jaramillo, J. K. Nørskov and J. Rossmeisl, *ChemCatChem*, 2011, **3**, 1159-1165.
42. R. H. Potze, G. A. Sawatzky and M. Abbate, *Physical Review B*, 1995, **51**, 11501-11506.
43. K. A. Stoerzinger, L. Qiao, M. D. Biegalski and Y. Shao-Horn, *J. Phys. Chem. Lett.*, 2014, **5**, 1636-1641.
44. N. K. Singh, S. K. Tiwari, K. L. Anitha and R. N. Singh, *J. Chem. Soc., Faraday Trans.*, 1996, **92**, 2397-2400.
45. Z. Lu, H. Wang, D. Kong, K. Yan, P.-C. Hsu, G. Zheng, H. Yao, Z. Liang, X. Sun and Y. Cui, *Nat. Commun.*, 2014, **5**.